4-Acetylantrocamol LT3 suppresses colorectal cancer growth and metastasis via PI3K/AKT and MAPK pathway modulation

KUEN-TZE LIN[1,2], YU-CHIEH HSIEH[3], PI-KAI CHANG[4,5], CHIH-WEI LAI[3], SHIH-YU LEE[6] and I-CHUAN YEN[3]

[1]Department of Radiation Oncology, Cardinal Tien Hospital, New Taipei City 23148, Taiwan, R.O.C.; [2]Graduate Institute of Aerospace and Undersea Medicine, National Defense Medical University, Taipei City 11490, Taiwan, R.O.C.; [3]School of Pharmacy, National Defense Medical University, Taipei City 11490, Taiwan, R.O.C.; [4]School of Medicine, National Defense Medical University, Taipei City 11490, Taiwan, R.O.C.; [5]Division of Colon and Rectal Surgery, Department of Surgery, Tri-Service General Hospital, National Defense Medical University, Taipei City 114202, Taiwan, R.O.C; [6]Department of Radiology, Taoyuan Armed Forces General Hospital, Taoyuan 325208, Taiwan, R.O.C.

Received July 24, 2025; Accepted December 16, 2025

DOI: 10.3892/ijmm.2026.5797

Abstract. Colorectal cancer (CRC) remains one of the leading causes of cancer-related mortality worldwide. Despite advances in targeted therapies, [2]drug resistance and limited efficacy in KRAS-mutant CRC continue to present clinical challenges. *Antrodia cinnamomea*, a medicinal fungus, demonstrates antitumor properties; however, the mechanisms of its triterpenoid compound, 4-acetylantrocamol LT3 (LT4), remain unclear. The present study investigated the effects of LT4 on KRAS-mutant HCT116 CRC cells using cell viability, colony formation and migration assays. Western blotting was also employed to examine key signaling pathways. Transcriptome profiling via RNA sequencing was followed by Kyoto Encyclopedia of Genes and Genomes/Gene Ontology enrichment and protein-protein interaction network analyses using STRING, CytoHubba and Molecular Complex Detection (MCODE). Molecular docking with PI3Kγ (PDB: 1E7U) was conducted to evaluate the predicted binding position and docking energy of LT4. The results indicated that LT4 significantly inhibited HCT116 cell proliferation and migration, induced a mesenchymal-to-epithelial transition, suppressed PI3K/AKT/mTOR and ERK signaling and activated the GSK3β/FOXO and phosphorylated-p38/p21 axes. LT4 also reduced the levels of cyclooxygenase-2 and anti-apoptotic proteins (Bcl-2 and Bcl-XL) and reduced the expression of the mitochondrial respiratory chain protein cytochrome c oxidase subunit IV. Transcriptomic analysis identified the PI3K/AKT pathway as the most significantly enriched signaling cascade. Network topology analyses highlighted solute carrier family 3 member 2, Cyclin D1, phosphoserine aminotransferase 1 and ChaC glutathione-specific γ-glutamylcyclotransferase 1 as central nodes, linking the effects of LT4 to nutrient signaling, redox homeostasis and serine metabolism. Molecular docking confirmed that LT4 stably occupied the ATP-binding pocket of PI3Kγ with a binding energy comparable to wortmannin and a conformation similar to antroquinonol. In conclusion, to the best of our knowledge, the present study is the first to comprehensively demonstrate the multi-target anti-CRC effects of LT4, highlighting its potential as a therapeutic agent, especially in KRAS-mutant CRC.

Correspondence to: Dr I-Chuan Yen, School of Pharmacy, National Defense Medical University, 161 Section 6, Minquan East Road, Neihu, Taipei City 11490, Taiwan, R.O.C.
E-mail: yenichuan@mail.ndmutsgh.edu.tw

Key words: *Antrodia cinnamomea*, 4-acetylantrocamol LT3, colorectal cancer, PI3K/AKT/mTOR, RNA sequencing, molecular docking, solute carrier family 3 member 2, Cyclin D1

Introduction

Colorectal cancer (CRC) is the third most commonly diagnosed malignancy worldwide and ranks as the second leading cause of cancer-related death, posing a significant global health burden (1). The incidence of CRC continues to rise, particularly in countries undergoing rapid industrialization and lifestyle changes (1). Despite advancements in screening programs and therapeutic strategies, the 5-year survival rate for patients with advanced or metastatic CRC remains ~16% (2,3). Current treatment modalities include surgical resection, chemotherapy (such as 5-fluorouracil-based regimens), radiotherapy and targeted therapies (such as anti-vascular endothelial growth factor and anti-epidermal growth factor receptor agents) (4). In recent years, immunotherapies, particularly immune checkpoint inhibitors targeting programmed cell death protein 1 and programmed death-ligand 1, have emerged as a promising option, especially for patients with high microsatellite instability or deficient mismatch repair tumors (4,5). However, these approaches are not universally effective; their efficacy is often limited by acquired resistance, genetic heterogeneity of the tumor and adverse side effects. Moreover, mutations in oncogenes and tumor suppressors such as KRAS, TP53 and APC, as well as aberrant activation of signaling pathways including Wnt/β-catenin, PI3K/AKT/mTOR and MAPK, are frequently implicated in disease progression and treatment resistance (6-8). These complexities underscore the urgent

need for complementary strategies targeting alternative molecular mechanisms to enhance therapeutic efficacy and reduce tumor recurrence.

In recent years, increasing attention has been directed toward the use of natural products and herbal medicines in cancer therapy. Owing to their multi-targeted mechanisms, lower toxicity profiles and historical usage in traditional medicine systems, natural compounds offer promising candidates for both chemoprevention and adjuvant therapy (9,10). Among these, *Antrodia cinnamomea* (commonly known as Niu-chang-chih), a medicinal fungus endemic to Taiwan, has gained significant scientific interest due to its wide spectrum of pharmacological activities, including anti-inflammatory, antioxidant, hepatoprotective, immunomodulatory and notably, anticancer effects (11). To date, research on *A. cinnamomea* has predominantly focused on its crude extracts, which have demonstrated inhibitory effects against various cancer types via multiple mechanisms, such as CHOP/tribbles pseudokinase 3 (TRB3)/AKT/mTOR pathway activation, suppression of NF-κB and c-Myc signaling and modulation of epithelial-mesenchymal transition (EMT) and tumor stemness (12-15). Despite these findings, research on the bioactivity of purified, structurally-defined compounds from *A. cinnamomea* remains limited, especially in the context of CRC. Among the active constituents, triterpenoids (particularly antcins) have shown anticancer potential across multiple malignancies, including oral, breast, pancreatic, prostate, ovarian, cervical and osteosarcoma models (16-18), and a few recent studies have begun to examine their effects in CRC. For example, antrodin C was reported to induce G1-phase arrest and apoptosis in HCT116 cells through reactive oxygen species (ROS)/AKT/ERK/p38 signaling and to suppress tumor growth in xenograft models (19). However, these studies remain largely descriptive, focusing on phenotypic outcomes such as apoptosis or cell-cycle arrest without elucidating the broader signaling networks or direct molecular targets involved.

The present study evaluated the anticancer potential of 4-acetylantrocamol LT3 (LT4), a purified triterpenoid derivative isolated from the mycelium of *A. cinnamomea*. Using human CRC HCT116 cells as a model, functional assays were performed in combination with transcriptomic profiling, protein expression analysis and molecular docking to elucidate the underlying mechanisms of LT4 action. The findings revealed novel insights into the signaling networks affected by LT4 and suggest that this compound may serve as a promising candidate for further development in CRC therapy.

Materials and methods

Preparation and purification of A. cinnamomea-derived compounds. In total, 4 compounds were isolated from *A. cinnamomea*, including dehydroeburicoic acid (DeEA) and dehydrosulphurenic acid (DSA) from the fruiting body and 4-acetylantroquinonol B (4AAQB) and LT4 from the mycelium. For DeEA and DSA, ethanolic extracts of the fruiting body were sequentially partitioned into hexane, ethyl acetate, dichloromethane and aqueous layers. Each layer was analyzed by reverse-phase high-performance liquid chromatography (HPLC) using aa Hitachi L-7100 instrument (Hitachi, Ltd.) equipped with a photodiode array detector (L-2400), a pump (L-2130) and an autosampler (L-2200). Separation was performed on a C18 column (Lichro CART® RP-18e; 4.0x250 mm i.d.; 5 μm; Merck KGaA) with the column temperature maintained at 25˚C. The mobile phase consisted of solvent A (0.1% formic acid in water) and solvent B (acetonitrile). The elution program was as follows: 0-3 min (A:B, 70:30 to 60:40), 3-15 min (A:B, 60:40 to 42:58), 15-21 min (A:B, 42:58), 21-26 min (A:B, 42:58 to 35:65), 26-35 min (A:B 35:65 to 0:100) and 35-50 min (0:100). The flow rate was 0.8 ml/min, the injection volume (sample quantity) was 10 μl and detection was performed at 254 nm. No internal standard was used. Based on the retention times, DSA and DeEA were identified at ~29 min and 45 min, respectively (Fig. S1A).

To isolate 4AAQB and LT4, the mycelial extract was subjected to reverse-phase HPLC using a Lichro CART® RP-18e column (4.0x250 mm, 5 μm; Merck KGaA) on a Hitachi L-7100 system equipped with a UV detector (L-7455). The column temperature was maintained at 25˚C. The mobile phase was a gradient of water-methanol: 40:60 for 15 min, 20:80 for 15 min and 0:100 for 10 min. The flow rate was 1.0 ml/min, the injection volume was 10 μl and the detection wavelength was 254 nm. No internal standard was used. The retention times were 14.92-15.35 min for 4AAQB, 17.93-17.97 min for antrocamol LT3 and 18.53-18.64 min for LT4, as confirmed by comparison with authentic standards (Fig. S1B-E).

Cell culture and authentication. Human CRC cell lines, HCT116 (KRAS mutant), HT-29 and Caco-2, were purchased from the American Type Culture Collection (ATCC; HCT116, CCL-247; HT-29, HTB-38; Caco-2, HTB-37). Cells were cultured in Dulbecco's Modified Eagle Medium (Gibco; Thermo Fisher Scientific, Inc.) supplemented with 10% fetal bovine serum (Gibco; Thermo Fisher Scientific, Inc.) and 1% penicillin-streptomycin and maintained in a humidified incubator at 37˚C with 5% CO_2. For routine experiments, cells were seeded at a density of $3x10^5$ to $6x10^5$ cells per 10-cm culture dish, unless otherwise specified. According to Cellosaurus, the HT-29 cell line (CVCL_0320) was originally derived from a rectosigmoid adenocarcinoma and should therefore be classified as a CRC cell line.

The cell lines were not independently authenticated in our laboratory but were obtained directly from ATCC and used within 6 months after resuscitation. Mycoplasma contamination was routinely monitored using PCR-based assays and found to be negative throughout the study.

Cell viability assay. HCT116, HT29 and Caco2 cells were seeded into 96-well plates at a density of $5x10^3$ cells/well and allowed to adhere overnight. The next day, the cells were treated with varying concentrations (0.1, 1, 3 or 10 μM) of DeEA, DSA, 4AAQB or LT4 for 24, 48 and 72 h. Cell viability was assessed using the Cell Counting Kit-8 (CCK-8; Dojindo Laboratories, Inc.). After treatment, CCK-8 solution was added to each well and the plates were incubated at 37˚C in a humidified atmosphere containing 5% CO_2 for 30 min. Absorbance was measured at 450/650 nm using a microplate reader (SpectraMax 190; Molecular Devices, LLC). Experiments were performed in triplicate.

Colony formation assay. HCT116 cells were seeded into 6-well plates at a density of 300 cells/well and allowed to adhere overnight at 37˚C in a humidified incubator with 5% CO_2. The following day, the cells were treated with LT4 at concentrations of 0, 0.1, 1, 3 or 10 μM and cultured for 10 days under the same conditions (37˚C, 5% CO_2). Colonies were fixed with 95% ethanol for 30 min at room temperature and stained with 1% crystal violet for another 30 min at room temperature. Excess dye was washed off with phosphate-buffered saline (PBS) and the plates were air-dried for 2-3 days. The colonies were imaged and quantification was performed by manual counting. A colony was defined as a cluster containing ≥50 cells.

Wound healing assay. HCT116 cells were seeded at $3x10^5$ cells/well into 6-well plates and cultured to near confluence. A uniform scratch was created using a 200 μl pipette tip and the cells were gently washed with PBS to remove debris. LT4 was added at final concentrations of 0, 0.1, 1, 3 or 10 μM in fresh serum-free medium. Images were captured using an inverted light microscope (phase-contrast) and the same microscopic fields were imaged at 0, 24, 48 and 72 h to monitor wound closure and cell migration. Wound closure was quantified using ImageJ (National Institutes of Health; v2.14.0/1.54f) by measuring the wound width at 0 h and at each indicated time point. For each image, the wound width was measured at multiple evenly spaced positions across the scratch and averaged to obtain a single value per well. The healing rate was calculated as $(W_0-W_t)/W_0$, where W_0 is the wound width at 0 h and W_t is the wound width at the indicated time.

RNA extraction. HCT116 cells were cultured in six 10 cm dishes until reaching confluence. Cells were divided into two groups: Three dishes for the control group and three dishes for the LT4-treated group (10 μM). The control group received an equal volume of DMSO [final concentration, 0.1% (v/v)] corresponding to the LT4 solvent. After 24 h of treatment, cells were washed 1-2 times with PBS to remove residual medium and avoid interference with the NucleoZOL reagent (Macherey-Nagel GmbH & Co. KG). Subsequently, at least 1 ml of NucleoZOL was added to each dish and the cells were scraped using a cell scraper. The lysates were transferred to centrifuge tubes, sealed with Parafilm to prevent leakage and stored at -20˚C or -80˚C.

For RNA purification, 400 μl of DEPC-treated water (NZYtech) was added per 1 ml of NucleoZOL lysate, followed by vigorous shaking for 15 sec and incubation at room temperature (18-25˚C) for 5-15 min. Samples were centrifuged at 12,000 x g for 15 min at 4˚C to separate the RNA-containing supernatant from the DNA/protein pellet. The supernatant was transferred to a new tube and 5 μl of 4-bromoanisole was added per 1 ml of supernatant for phase separation. After mixing for 15 sec and incubating at room temperature for 35 min, samples were centrifuged at 12,000 x g for 10 min at 4˚C. The RNA-containing supernatant was then mixed with an equal volume of isopropanol to precipitate RNA, incubated at room temperature for 10 min and centrifuged at 12,000 x g for 10 min. The RNA pellet was washed twice with 75% ethanol, centrifuged at 4,000-8,000 x g for 1-3 min at 4˚C and air-dried briefly. Finally, RNA was dissolved in DEPC-treated water to achieve a concentration of 1-2 μg/μl and incubated at room temperature for 2-5 min to ensure complete dissolution.

RNA sequencing (RNA-seq) and bioinformatic analysis. RNA-seq was performed by Genomics, BioSci & Tech Co., Ltd. (New Taipei City, Taiwan). Library preparation followed the TruSeq Stranded mRNA Library Prep Kit protocol (Illumina, Inc.). Briefly, 1 μg of total RNA was used to isolate mRNA using oligo(dT) magnetic beads, followed by fragmentation and synthesis of first and second-strand cDNA. After end repair, 3' adenylation and adaptor ligation, libraries were amplified by PCR and purified using AMPure XP beads (Beckman Coulter, Inc.). Library quality was assessed using the Agilent 2100 BioAnalyzer, and quantification was performed using quantitative PCR. Sequencing was conducted on the Illumina NovaSeq X Plus platform using a NovaSeq X Series 10B Reagent Kit (300-cycle; Illumina, Inc.) to generate 150-bp paired-end reads. The final pooled library was diluted and loaded at an average concentration of 110 pM according to the manufacturer's recommendations. RNA-seq data have been deposited in the NCBI Gene Expression Omnibus under accession no. GSE299648.

Raw sequencing data were converted to FASTQ format using bcl2fastq (v2.20.0; Illumina, Inc.). Sequencing reads were processed using fastp (v0.20.0) to remove low-quality reads and adapters (20). Ribosomal RNA filtering is an optional step and was not performed in this study (that is, no SortMeRNA filtering). Trimmed sequences were aligned to the human reference genome GRCh38 (RefSeq assembly: GCF_000001405.40; https://www.ncbi.nlm.nih.gov/datasets/genome/GCF_000001405.40/) using HISAT2 (v2.1.0; Johns Hopkins University; https://daehwankimlab.github.io/hisat2/). The resulting SAM files were converted to BAM format using SAMtools (v1.9; SAMtools project; https://www.htslib.org/). Gene-level read counts were calculated using featureCounts (Subread v2.0.1; Subread package; http://subread.sourceforge.net/) and normalized to transcripts per million. Differentially expressed genes (DEGs) were identified using DESeq2 (v1.48.2) with thresholds set at $|\log_2$ fold change$|\geq 1$ and adjusted $P<0.05$ (21). Gene Ontology (GO) and Kyoto Encyclopedia of Genes and Genomes (KEGG) enrichment analyses were performed using clusterProfiler (v4.12.6) (22).

Western blotting. Proteins were extracted using RIPA buffer prepared in-house (150 mM NaCl, 1% NP-40, 0.1% SDS, 50 mM Tris-HCl pH 7.6, 10 mM EDTA pH 8.0 and 0.5% sodium deoxycholate), supplemented with 1 M PMSF (Sigma-Aldrich; Merck KGaA) and phosphatase inhibitors (1 mM Na_3VO_4, 10 mM NaF and 10 mM β-glycerophosphate). Protein concentrations were determined using the BCA assay (Pierce; Thermo Fisher Scientific, Inc.). Equal amounts of protein (30 μg) were separated by 10% SDS-PAGE and transferred onto PVDF membranes (MilliporeSigma). After blocking with 5% non-fat milk for 30 min at 25˚C, membranes were incubated overnight at 4˚C with the indicated primary antibodies. Most primary antibodies, including those against phosphorylated (p-)AKT (Ser473) (cat. no. 4060), AKT (cat. no. 9272), p-mTOR (Ser2448) (cat. no. 5536), mTOR (cat. no. 2983), p-PI3K p85 (Tyr458) (cat. no. 4228), PI3K p85

(cat. no. 4257), p-ERK1/2 (Thr202/Tyr204) (cat. no. 4370), ERK1/2 (cat. no. 4695), p-p38 (Thr180/Tyr182) (cat. no. 4511), p38 (cat. no. 9212), GSK3β (cat. no. 12456), p-GSK3β (Ser9) (cat. no. 5558), FOXO3a (cat. no. 2497), FOXO1 (cat. no. 2880), p-FOXO1 (Ser256) (cat. no. 9461), $p27^{kip1}$ (cat. no. 3686), $p21^{Cip1/Waf1}$ (cat. no. 2947), cyclooxygenase-2 (COX-2; cat. no. 12282), Bcl-2 (cat. no. 4223), Bcl-XL (cat. no. 2764), Bax (cat. no. 2772), cytochrome c oxidase subunit IV (COX IV; cat. no. 4850), β-actin (cat. no. 4970), N-cadherin (cat. no. 13116) and E-cadherin (cat. no. 3195) were purchased from Cell Signaling Technology, Inc. [rabbit host; diluted 1:1,000 in 5% BSA (Sigma-Aldrich; Merck KGaA)/PBST (PBS containing 0.1% Tween-20) with 1% NaN_3]. The anti-Vimentin antibody (cat. no. ARG66199) was obtained from Arigo Biolaboratories Corp. and used under the same dilution and buffer conditions as aforementioned. After incubation with HRP-conjugated goat anti-rabbit secondary antibody (Abcam; cat. no. ab6721; 1:10,000 in 5% milk), membranes were washed and developed using enhanced chemiluminescence (Thermo Fisher Scientific, Inc.). Band intensities were semi-quantified using ImageJ (v1.50a) and all experiments were performed in triplicate.

Protein-protein interaction (PPI) network analysis. DEGs were analyzed using the STRING database (https://string-db.org/) to construct PPI networks, with a confidence score ≥0.4. The resulting networks were visualized using Cytoscape (v3.10.2; Cytoscape Consortium; https://cytoscape.org/), and key hub genes were identified using the CytoHubba plugin, which applies 11 topological analysis methods, including Degree, maximal clique centrality (MCC) and maximum neighborhood component (MNC). Additionally, the MCODE plugin was used to detect densely connected regions within the network, with parameters set as follows: Degree cut-off=2, node score cut-off=0.2 and K-Core=2.

Molecular docking. Molecular docking studies were conducted using BIOVIA Discovery Studio 2024 Client (BIOVIA; v24.1.0.23298; Dassault Systèmes S.E.). The crystal structure of PI3Kγ (PDB ID: 1E7U) was retrieved from the RCSB Protein Data Bank (https://www.rcsb.org/structure/1E7U) and was originally reported by Walker *et al* (23). Protein preparation involved removal of water molecules and the addition of hydrogen atoms. Ligand structures for antroquinonol and wortmannin were obtained from PubChem (https://pubchem.ncbi.nlm.nih.gov/compound/24875259 and https://pubchem.ncbi.nlm.nih.gov/compound/312145, respectively). The 2D structure of LT4 was drawn using ChemDraw Prime (v23; Revvity Signals Software). Energy minimization was performed. Docking simulations were carried out using the CDOCKER algorithm, focusing on the ATP-binding site of PI3Kγ. Binding energies and interaction modes were analyzed and docking poses were visualized using PyMOL (v3.1; Schrödinger, LLC; https://pymol.org/) and BIOVIA Discovery Studio Client.

Statistical analysis. Data are expressed as mean ± SD, except for the molecular binding energy results, which are presented as mean ± SEM. Group differences in docking energies were assessed using unpaired t-tests. Other experimental data were analyzed by one-way ANOVA followed by Bonferroni post hoc tests. $P<0.05$ was considered to indicate a statistically significant difference. All statistical analyses were performed using SPSS Statistics (v22.0; IBM Corp.). Graphs and quantifications were generated using GraphPad Prism (v5.0; Dotmatics) and ImageJ. All experiments were performed in at least triplicate (n≥3).

Results

Lt4 selectively inhibits the viability of KRAS-mutant HCT116 CRC cells. To evaluate the anticancer potential of four compounds derived from *A. cinnamomea*, including DeEA and DSA from the fruiting body and 4AAQB and LT4 from the mycelium, cell viability assays with three human CRC cell lines, HCT116 (KRAS mutant) and HT29 and Caco2 (both KRAS wild-type), were conducted. Cells were treated with increasing concentrations of each compound (0.1, 1, 3 and 10 μM) and cell viability was assessed at 24, 48 and 72 h using the CCK-8 assay (Fig. 1A-C).

Among the four compounds tested, LT4 and 4AAQB showed the most evident inhibitory effects on HCT116 cell viability, whereas DeEA and DSA produced minimal changes under the same conditions (Fig. 1A). Notably, LT4 exhibited a clearer dose- and time-associated decrease, reaching statistical significance at concentrations ≥1 μM at later time points (Fig. 1A, bottom right panel). Although 4AAQB also caused significant reductions in viability in HCT116 cells, the overall pattern was less consistent across time points compared with LT4 (Fig. 1A, bottom left panel). In HT29 and Caco2 cells, the viability responses to LT4 and 4AAQB were cell line-dependent, showing generally milder inhibition than that observed in HCT116 cells (Fig. 1B and C). Notably, Caco2 cells exhibited a comparable reduction in viability in response to 4AAQB and LT4 (Fig. 1C). Given the clearer overall inhibitory trend of LT4 in KRAS-mutant HCT116 cells, LT4 was selected for downstream mechanistic investigations.

LT4 inhibits colony formation, cell migration and EMT in HCT116 cells. To further assess the anti-proliferative effects of LT4 on CRC cells, a colony formation assay with HCT116 cells treated with LT4 (0.1-10 μM) for 14 days was performed. As shown in Fig. 2A, LT4 significantly suppressed the clonogenic potential of HCT116 cells in a dose-dependent manner, particularly at concentrations of ≥1 μM.

To investigate the effect of LT4 on cell migration, a wound healing assay was next conducted. Compared with the control group, LT4 treatment markedly inhibited cell migration in a time- and dose-dependent manner (Fig. 2B). Quantification of the healing rates revealed that 3 and 10 μM LT4 significantly delayed wound closure at both 48 and 72 h.

Given that EMT plays a pivotal role in cancer invasion and metastasis (24), the expression levels of EMT markers in LT4-treated HCT116 cells were examined. Densitometric analysis of three independent western blot experiments showed that LT4 reduced the levels of the mesenchymal marker N-cadherin, reaching statistical significance at 10 μM (Fig. 2C), while significantly upregulating the epithelial marker E-cadherin at 1-3 μM (Fig. 2D). To strengthen the EMT assessment, Vimentin was also measured, a canonical mesenchymal marker widely used in CRC EMT studies (25-28). Densitometric analysis of western blots showed that LT4 significantly reduced Vimentin

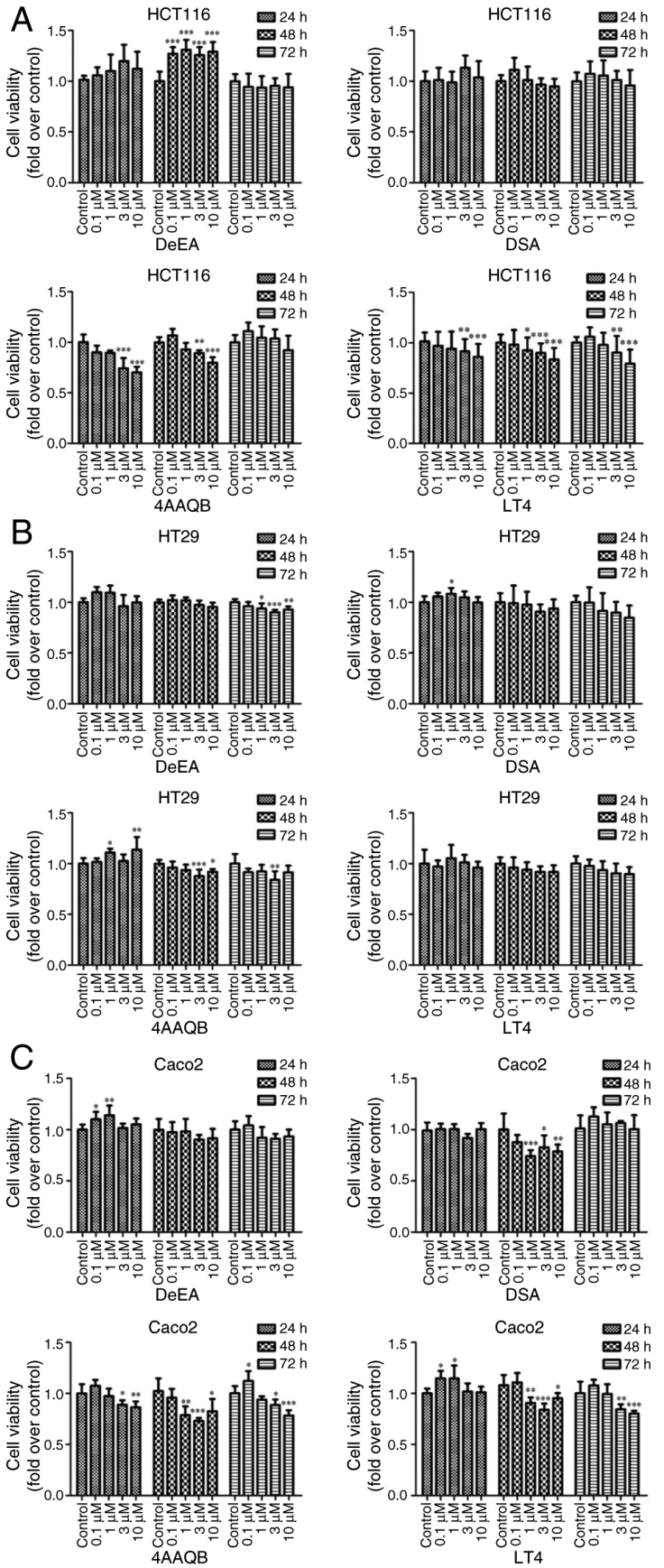

Figure 1. Effects of four *Antrodia cinnamomea*-derived triterpenoid compounds on CRC cell viability. Cell viability was assessed by Cell Counting Kit-8 assay in three human CRC cell lines: (A) HCT116 (KRAS mutant), (B) HT29 (KRAS wild-type) and (C) Caco-2 (KRAS wild-type) after treatment with increasing concentrations (0.1, 1, 3 and 10 μM) of DeEA, DSA, 4AAQB and LT4 for 24, 48 and 72 h. Absorbance was recorded at 450/650 nm and normalized to vehicle-treated controls (0.1% DMSO). Data are presented as the mean ± SD from at least three independent experiments (n≥3). *P<0.05, **P<0.01, ***P<0.001 vs. vehicle-treated control. CRC, colorectal cancer; DeEA, dehydroeburicoic acid; DSA, dehydrosulphurenic acid; 4AAQB, 4-acetylantroquinonol B; LT4, 4-acetylantrocamol LT3.

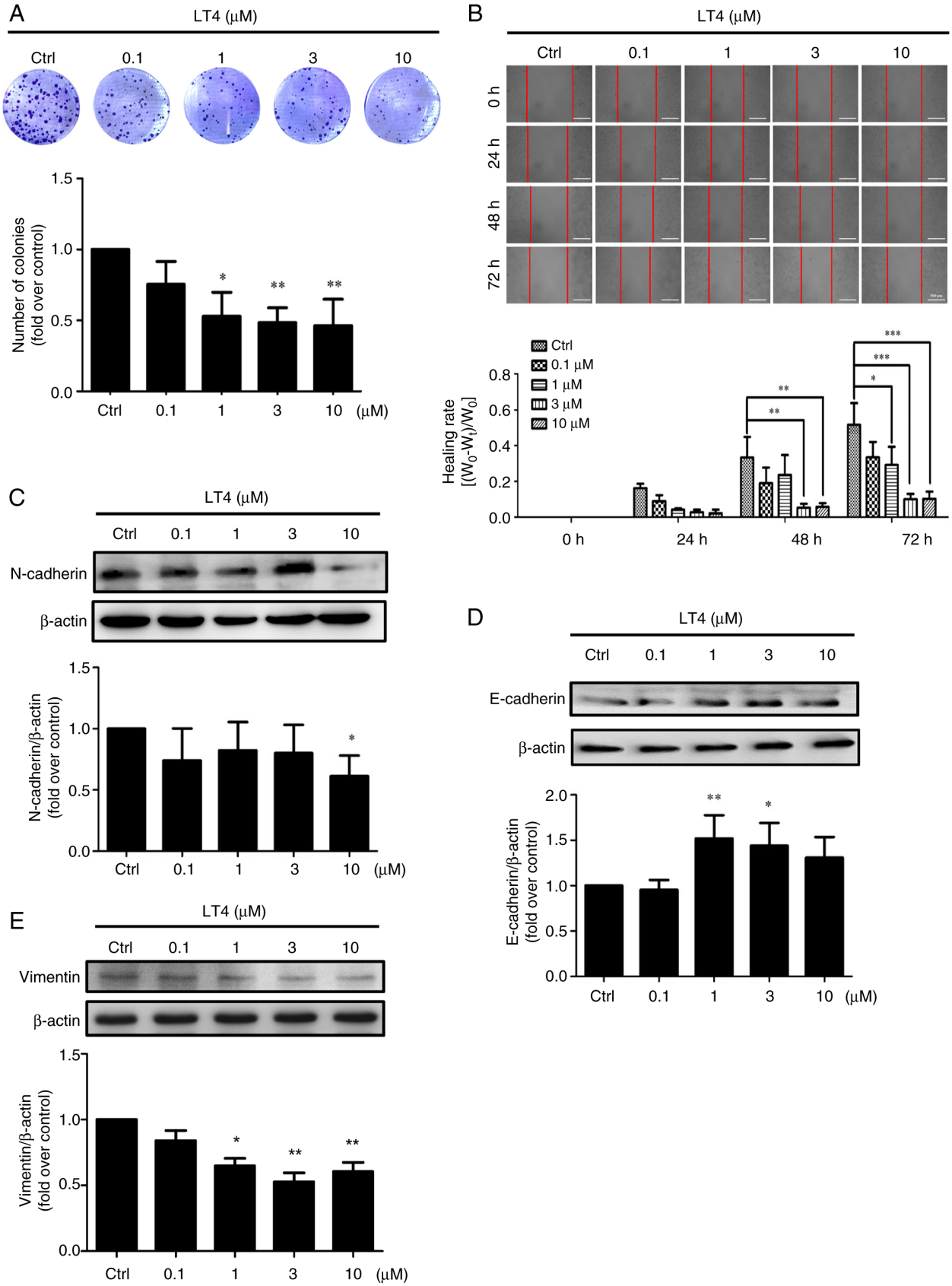

Figure 2. LT4 suppresses colony formation, cell migration and EMT in HCT116 cells. (A) Colony formation assay was performed after treating HCT116 cells with various concentrations of LT4 (0.1, 1, 3 and 10 μM) for 14 days. Colonies were stained with crystal violet and quantification of colony growth was calculated relative to the vehicle-treated Ctrl. (B) Wound healing assay showing inhibition of cell migration by LT4 (0.1, 1, 3 and 10 μM) at 24, 48 and 72 h post-scratch. Representative images and quantified healing rates are shown. Western blot analysis of EMT-related proteins (C) N-cadherin (140 kDa), (D) E-cadherin (130 kDa) and (E) Vimentin (54 kDa) in HCT116 cells after 24-h LT4 treatment (0.1, 1, 3 and 10 μM). β-actin (45 kDa) served as the loading control. The corresponding bar graphs show semi-quantification of N-cadherin/β-actin, E-cadherin/β-actin and vimentin/β-actin expressed as fold change relative to the vehicle-treated Ctrl. Data are presented as the mean ± SD from three independent experiments (n=3). *P<0.05, **P<0.01, ***P<0.001 vs. vehicle-treated Ctrl. LT4, 4-acetylantrocamol LT3; EMT, epithelial-mesenchymal transition; Ctrl, control.

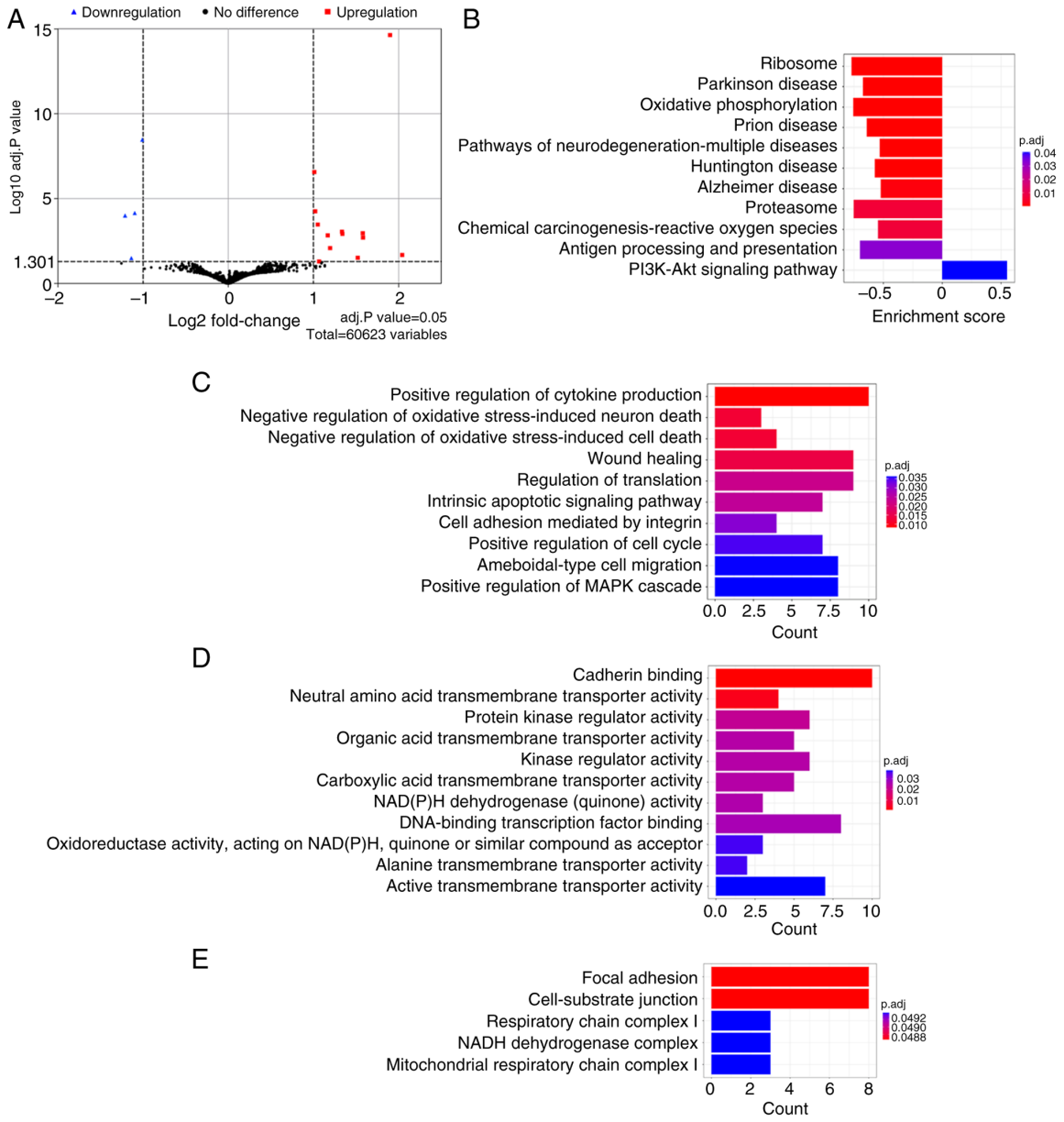

Figure 3. Transcriptomic analysis of LT4-treated HCT116 cells reveals modulation of tumor-associated pathways. (A) Volcano plot illustrating DEGs in HCT116 cells treated with LT4 (10 μM, 24 h) compared with the control. DEGs were defined using thresholds of $|\log_2(\text{fold change})| \geq 1$ and adjusted P<0.05. Red dots indicate significantly upregulated genes; blue dots indicate significantly downregulated genes (adjusted P<0.05). (B) Kyoto Encyclopedia of Genes and Genomes pathway enrichment analysis of DEGs. The x-axis represents the enrichment score, defined as the ratio of DEG counts to background counts for each pathway (log-transformed), with positive values indicating enrichment. Gene Ontology enrichment analysis of DEGs based on (C) Biological Process, (D) Molecular Function and (E) Cellular Component. Data are expressed as enrichment score or DEG counts. LT4, 4-acetylantrocamol LT3; DEGs, differentially expressed genes.

protein expression at 1-10 μM, with the lowest level observed at 3 μM (Fig. 2E). Together, these results suggest that LT4 not only impaired proliferation and migration but also suppressed EMT phenotypes in HCT116 CRC cells by downregulating mesenchymal markers and restoring epithelial features.

LT4 treatment alters gene expression profiles and enriches the PI3K/AKT and MAPK pathways in HCT116 cells. To investigate the transcriptional changes induced by LT4 in CRC cells, RNA-seq was performed on HCT116 cells treated with 10 μM LT4 for 24 h. The complete RNA-seq output for all transcripts detected in LT4-treated and control HCT116 cells is provided in Table SI. DEGs were identified using a cut-off of $|\log_2(\text{fold change})| \geq 1$ and adjusted P<0.05 (corresponding to $-\log_{10}(\text{P-adjust}) \geq 1.3$), yielding a total of 17 DEGs (13 upregulated and 4 downregulated) in LT4-treated HCT116 cells, as visualized by volcano plot (Fig. 3A). Among the upregulated genes were ZNF460, CHAC1, KIF21A, FBXO30, KLHL11, SLC7A11, CLIC4, NT5E, CPA4, BCAN-AS2, AHNAK, UPP1 and AKAP12, while ND6, PLEKHO1, KRT13 and CRABP2 were significantly downregulated. Detailed information on the DEGs is provided in Table SII.

To elucidate the functional relevance of these DEGs, KEGG and GO enrichment analyses were performed. KEGG pathway analysis revealed significant enrichment in 'PI3K-Akt signaling pathway', 'Antigen processing and presentation' and 'Chemical carcinogenesis-reactive oxygen species' (Fig. 3B). GO enrichment in the Biological Process category highlighted

terms such as 'Positive regulation of cytokine production', 'Wound healing', 'Ameboidal-type cell migration', 'Positive regulation of MAPK cascade' and 'Intrinsic apoptotic signaling pathway' (Fig. 3C). In the Molecular Function category, enriched annotations included 'Cadherin binding', 'DNA-binding transcription factor binding', 'Protein kinase regulator activity' and 'Active transmembrane transporter activity' (Fig. 3D). GO analysis of Cellular Components further revealed enrichment in 'Focal adhesion' and 'Cell-substrate junction', structures essential for cell adhesion and signaling (Fig. 3E). These results suggest that LT4 modulates key gene expression programs associated with tumor survival, migration, stress adaptation and oncogenic signaling in CRC cells.

Construction of a PPI network and identification of hub genes. To elucidate the interaction landscape of LT4-responsive genes, a PPI network was constructed using the STRING database. A total of 83 significantly regulated genes (adjusted $P<0.05$ without applying the $|\log2FC|\geq1$ threshold) were submitted to STRING to avoid an overly sparse network and to retain sufficient nodes for module/hub analysis, and 63 genes with non-zero node degree were retained for network visualization and further analysis (Fig. 4A; Table SIII for the full STRING node list). The network comprised 113 interactions, filtered with a confidence score threshold >0.4.

To prioritize key regulatory genes within this network, topological analysis was performed using the CytoHubba plugin in Cytoscape. Based on integrated centrality scores across 11 parameters, including Degree, MCC, MNC, DMNC, Closeness, Betweenness and others (Fig. S2; Table SIV for detailed CytoHubba centrality rankings), several high-ranking hub genes were identified, such as solute carrier family 3 member 2 (SLC3A2), Cyclin D1 (CCND1), phosphoserine aminotransferase 1 (PSAT1), ChaC glutathione-specific γ-glutamylcyclotransferase 1 (CHAC1), TRIB3 and ITGB1, which appeared in the top-10 lists across multiple ranking methods (Fig. 4B).

Further clustering analysis was performed using the MCODE plugin to identify densely connected modules within the PPI network. In total, 4 distinct clusters were identified and are summarized in Fig. 4C. Cluster 1 had the highest score (4.0), consisting of 6 tightly interconnected nodes: SLC3A2, SLC7A11, SLC38A1, ATF4, CHAC1 and PSAT1. These genes are associated with amino acid transport, oxidative stress response and cellular metabolism (29-33). Other clusters encompassed mitochondrial respiratory components and ribosome-related genes, indicating LT4-induced modulation of metabolic and proliferative signaling hubs. These clustering results closely aligned with the CytoHubba analysis, reinforcing the biological relevance of these modules.

Taken together, these findings highlight a functional hub centered around SLC3A2 and CCND1, linking nutrient sensing, redox regulation and cell cycle progression, potentially mediating the anticancer effects of LT4 in CRC cells.

LT4 suppresses PI3K/AKT/mTOR and PI3K/AKT/GSK3β/FOXO signaling pathways in HCT116 cells. Network analysis identified SLC3A2 and CCND1 as 2 key hub genes in LT4-treated CRC cells. Both genes have been implicated in cancer progression. For instance, SLC3A2 (also known as CD98hc) is a transmembrane amino acid transporter that has been reported to be upregulated in various cancer types, including osteosarcoma, lung, breast and biliary tract cancer, where it contributes to tumor proliferation and invasion, primarily through the PI3K/AKT signaling pathway (34-39), and in certain contexts via ERBB2/ERBB3-mediated MAPK activation (40). In CRC, SLC3A2 depletion has been shown to suppress cell proliferation and metastasis through the AKT/GSK-3β pathway and induction of ferroptosis (41). CCND1, a key regulator of the G1/S cell cycle transition, is frequently upregulated in colon, breast and gastric cancer (42-44); it serves as a downstream effector of multiple oncogenic cascades, including PI3K/AKT/mTOR and AKT/GSK3β, promoting cell cycle progression and tumor growth (45-47).

To further elucidate whether LT4 targets these signaling cascades, western blotting was performed to assess the PI3K/AKT/mTOR and PI3K/AKT/GSK3β/FOXO axes. In LT4-treated HCT116 cells, the phosphorylation levels of PI3K (p85), AKT (Ser473) and mTOR were significantly reduced in a dose-dependent manner, while total PI3K, AKT and mTOR levels remained unchanged (Fig. 5A-D). These results demonstrated that LT4 inhibited the PI3K/AKT/mTOR signaling pathway, a key regulator of cell growth and protein synthesis.

The downstream targets of AKT were next evaluated. Densitometric quantification of three independent western blot experiments showed that LT4 increased FOXO3a protein levels, reaching statistical significance at 3-10 μM (Fig. 6A and B), and increased $p27^{kip1}$ levels at 1 and 10 μM (Fig. 6A and C), both of which have been implicated in tumor suppression (48,49). In parallel, the p-FOXO1/FOXO1 ratio was reduced at 10 μM (Fig. 6D and E). Moreover, LT4 increased the p-GSK3β/GSK3β ratio, with a significant peak at 1 μM (Fig. 6D and F). Collectively, these findings indicated that LT4 modulated the PI3K/AKT/GSK3β/FOXO pathway, leading to cell cycle inhibition and enhanced apoptotic potential in CRC cells.

LT4 suppresses the ERK branch of the MAPK pathway while activating the p38-p21 axis and reducing COX-2 expression. Given that LT4 inhibits the PI3K/AKT/mTOR and GSK3β/FOXO axes, both crucial for cell cycle regulation, it was next investigated whether MAPK signaling, another central pathway regulating proliferation and stress response, is also modulated by LT4.

As shown in Fig. 7A, LT4 treatment markedly decreased p-ERK levels in a dose-dependent manner, while total ERK remained unchanged. Semi-quantification confirmed significant suppression of ERK activation at all tested concentrations (Fig. 7B), indicating that LT4 inhibited the ERK arm of MAPK signaling, potentially reducing proliferative signaling. Notably, the level of p-p38 MAPK, another branch of the MAPK pathway often associated with cellular stress responses, was significantly upregulated at 3 μM LT4 (Fig. 7D). This shift may reflect a compensatory response or cell cycle regulatory mechanism. Consistent with this, the expression of p21, a cyclin-dependent kinase inhibitor and downstream target of both ERK and p38 (50-52), was markedly elevated in a dose-dependent manner, with the highest expression at 10 μM (Fig. 7A and C). Collectively, these findings indicate that LT4 activated the p38-p21 axis, thereby promoting p21-mediated

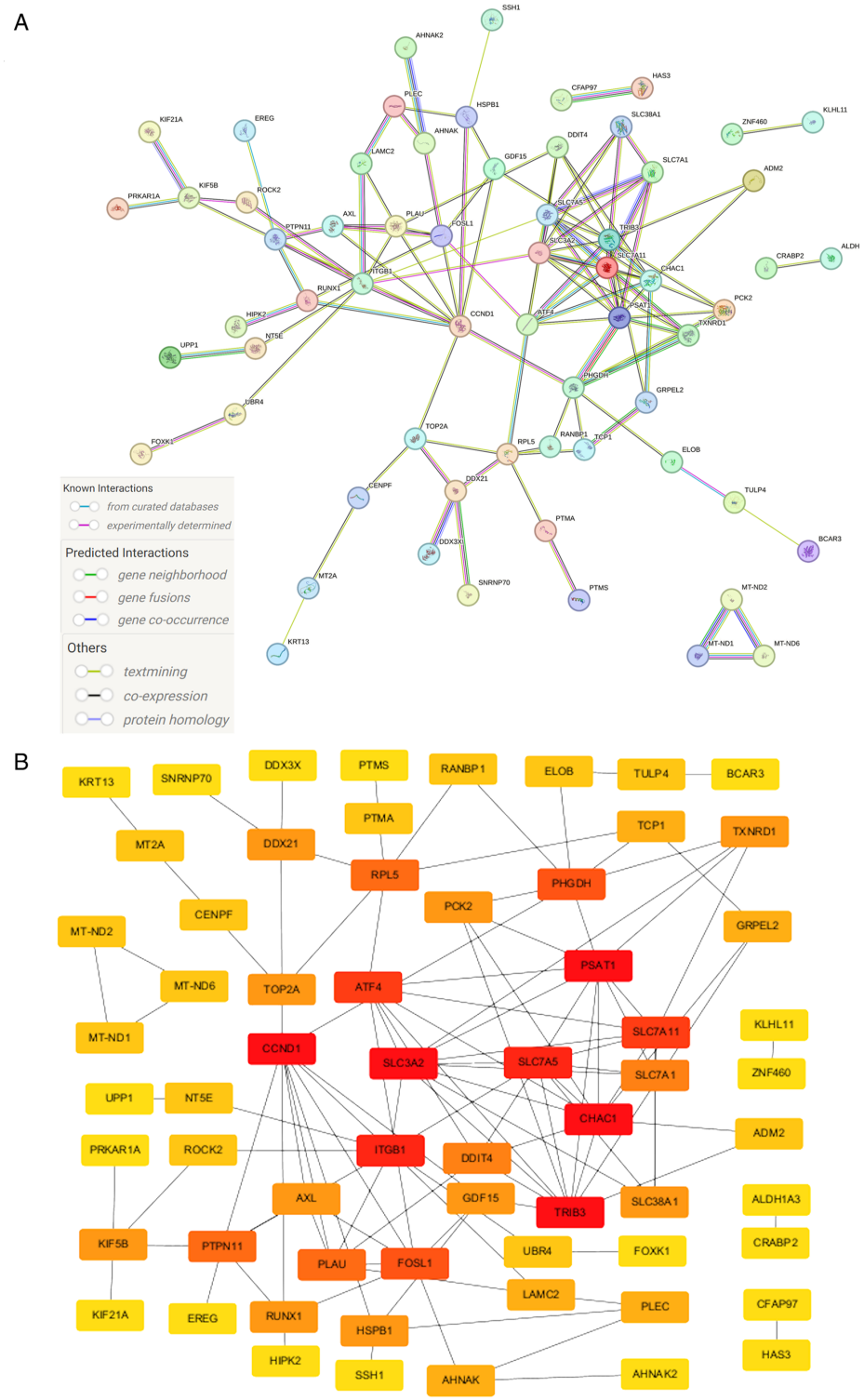

Cluster	Score (Density*#Nodes)	Nodes	Edge	Node IDs
1	4	6	6	SLC3A2, SLC7A1, SLC38A1, ATF4, CHAC1, PSAT1
2	3	3	3	FOSL1, PLAU, AXL
3	3	3	3	MT-ND6, MT-ND2, MT-ND1
4	2.8	6	6	CCND1, DDX21, GDF15, RPL5, TOP2A, HSPB1

Figure 4. PPI network and hub gene analysis of LT4-regulated DEGs in HCT116 cells. (A) PPI network of 63 DEGs (adjusted P<0.05) with non-zero node degree, constructed using the STRING database. Node-node interactions were filtered at a medium confidence level (interaction score ≥0.4). Known and predicted protein interactions are indicated by colored edges. (B) Network of key hub genes identified using CytoHubba topological analysis in Cytoscape. Node color intensity reflects centrality values (red=higher centrality). (C) MCODE analysis identified four gene clusters based on connectivity density. Each cluster is defined by its score (calculated as the product of subnetwork density and number of nodes), node count and edge count (number of interactions within the cluster). See Table SIII for the full STRING node list and Fig. S2 for detailed CytoHubba centrality rankings. PPI, protein-protein interaction; LT4, 4-acetylantrocamol LT3; DEGs, differentially expressed genes; MCODE, Molecular Complex Detection.

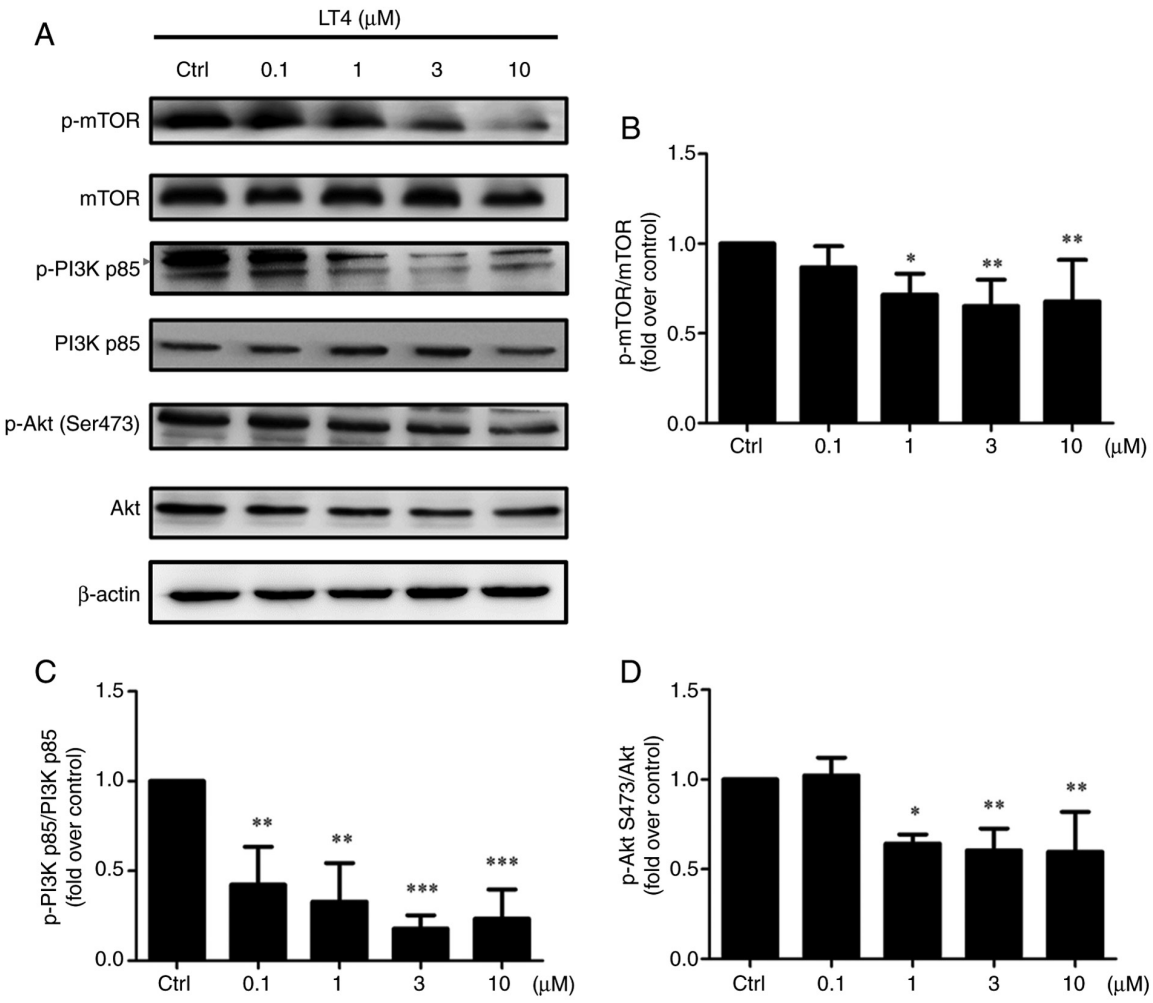

Figure 5. LT4 inhibits PI3K/AKT/mTOR signaling in HCT116 cells. (A) Western blot analysis of p-PI3K (p85, 85 kDa), total PI3K, p-AKT (Ser473, 60 kDa), total AKT, p-mTOR (289 kDa) and total mTOR in cells treated with LT4 (0.1, 1, 3 and 10 μM) for 24 h. β-actin (45 kDa) served as the loading control. Semi-quantification of (B) p-mTOR/mTOR, (C) p-PI3K p85/PI3K p85 and (D) p-AKT (Ser473)/AKT. Data are presented as the mean ± SD from three independent experiments. Representative blots are shown; bar graphs represent densitometric quantification from three independent experiments (n=3), normalized to the indicated total protein, and expressed as fold change relative to the vehicle-treated Ctrl. *P<0.05, **P<0.01, ***P<0.001 vs. vehicle-treated Ctrl. LT4, 4-acetylantrocamol LT3; p-, phosphorylated; Ctrl, control.

cell cycle arrest (51,53), while simultaneously dampening ERK-mediated proliferative signaling.

To further clarify the anti-proliferative and pro-apoptotic mechanisms of LT4, its effect on COX-2, a known downstream effector of both the PI3K/AKT and MAPK pathways and a pro-tumorigenic factor in CRC, was examined (54-56). Western blot analysis demonstrated a consistent, dose-dependent decrease in COX-2 protein levels following LT4 treatment (Fig. 7E and F), suggesting that LT4 may suppress inflammatory and survival pathways downstream of ERK and PI3K.

Together, these results support a model in which LT4 modulates multiple MAPK signaling branches to reduce proliferation (via ERK inhibition and COX-2 suppression) and induce cell cycle arrest (via p38-mediated p21 upregulation), complementing its effects on PI3K/AKT signaling.

LT4 modulates the levels of Bcl-2 family proteins and the mitochondrial marker COX IV in HCT116 cells. Since both p38 MAPK and the PI3K/AKT/GSK3β/FOXO axis are known to regulate apoptotic signaling (57-64), it was next investigated whether LT4 treatment modulated Bcl-2 family protein expression in HCT116 cells. As shown in Fig. 8A and B, Bcl-XL levels showed no significant changes across the tested concentrations. By contrast, Bcl-2 was significantly reduced at 3 μM LT4 (Fig. 8C). Conversely, the expression of the pro-apoptotic protein Bax was significantly increased at 1 μM (Fig. 8D), consistent with a shift toward a pro-apoptotic Bcl-2/Bax balance following LT4 exposure. To further investigate whether LT4 also affects mitochondrial-associated protein expression, the expression of COX IV, a mitochondrial inner membrane protein commonly used as a mitochondrial marker (65), was assessed. COX IV expression was slightly but significantly reduced at 10 μM (Fig. 8A and E), suggesting that high-dose LT4 may alter mitochondrial-associated protein levels. Together, these data indicate that LT4 shifts Bcl-2 family protein expression toward a pro-apoptotic profile and is accompanied by a reduction in the mitochondrial marker COX IV at higher concentrations, suggesting possible involvement of mitochondrial-associated apoptotic signaling.

Molecular docking suggests LT4 stably binds to the ATP-binding pocket of PI3Kγ. Among the numerous signaling

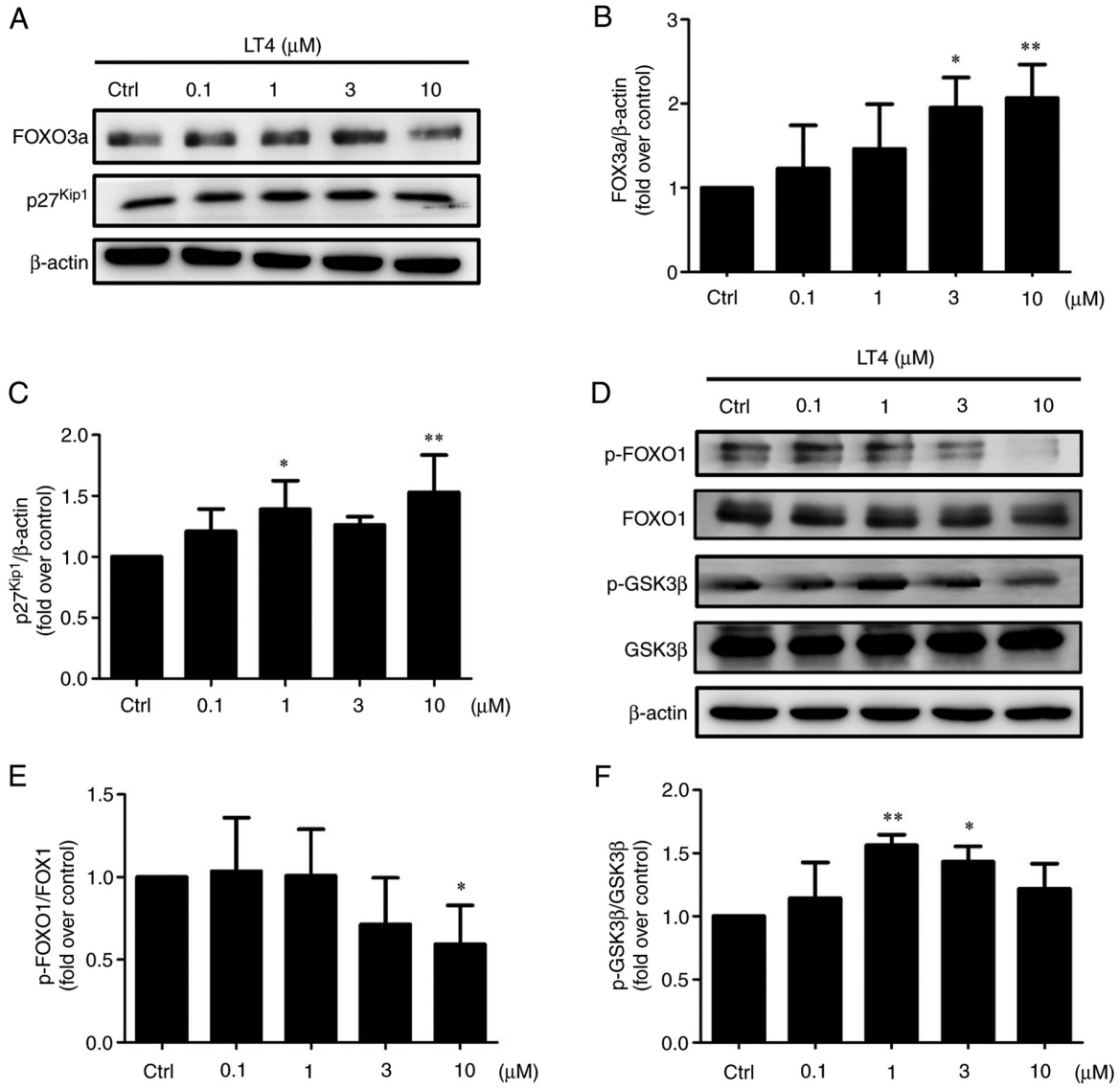

Figure 6. LT4 modulates downstream PI3K/AKT signaling via FOXO3a, $p27^{kip1}$, FOXO1 and GSK3β in HCT116 cells. HCT116 cells were treated with LT4 (0.1, 1, 3 and 10 μM) for 24 h, followed by western blotting and densitometric analysis. (A) Representative western blots of FOXO3a (82-97 kDa) and $p27^{kip1}$ (27 kDa), with β-actin (45 kDa) as the loading control. (B) Densitometric quantification of FOXO3a/β-actin. (C) Densitometric quantification of $p27^{kip1}$/β-actin. (D) Representative western blots of p-FOXO1 (Ser256), total FOXO1 (78-82 kDa), p-GSK3β (Ser9) and total GSK3β (46 kDa). β-actin (45 kDa) served as the loading control. (E) Densitometric quantification of p-FOXO1/FOXO1. (F) Densitometric quantification of p-GSK3β/GSK3β. Data are presented as the mean ± SD from three independent experiments. Bar graphs represent densitometric quantification from three independent experiments (n=3), normalized to the indicated total protein or β-actin, and expressed as fold change relative to the vehicle-treated Ctrl. *P<0.05, **P<0.01 vs. vehicle-treated Ctrl. LT4, 4-acetylantrocamol LT3; p-, phosphorylated; Ctrl, control.

components modulated by LT4, PI3K appeared as a central regulatory node. Western blot analysis showed consistent and robust inhibition of phosphorylated PI3K (p85 subunits), while transcriptomic KEGG enrichment further supported the PI3K/AKT pathway as one of the most significantly affected signaling cascades. GO terms related to kinase regulation, focal adhesion and cell cycle regulation likewise pointed toward upstream PI3K involvement. To validate whether PI3K could serve as a direct target of LT4, a molecular docking study was conducted using PI3Kγ (PDB ID: 1E7U) as the receptor template. The 1E7U structure represents a co-crystallized complex of PI3Kγ with wortmannin (KWT), a classical covalent inhibitor of PI3K, enabling precise definition of the ATP-binding pocket (23). Antroquinonol, a structural analogue of LT4 derived from *A. cinnamomea* and previously shown to exhibit anti-CRC activity, was included as a natural compound comparator (66,67).

Since the receptor structure (PDB ID: 1E7U) contains a co-crystallized KWT complex, KWT was first removed and re-docked as a positive control to validate the docking settings and pocket definition. Using the same grid and parameters, antroquinonol and LT4 were then docked into the PI3Kγ ATP-binding pocket to enable a head-to-head comparison of predicted binding modes and binding energies under identical conditions. The original PI3Kγ-wortmannin co-crystal structure was reported by Walker *et al* (23). Docking simulations revealed that KWT bound deeply within the ATP-binding cleft of PI3Kγ, forming key interactions with residues such as Val-882 and Lys-890 (Fig. 9A and B). Antroquinonol displayed stable binding by forming a hydrogen bond with

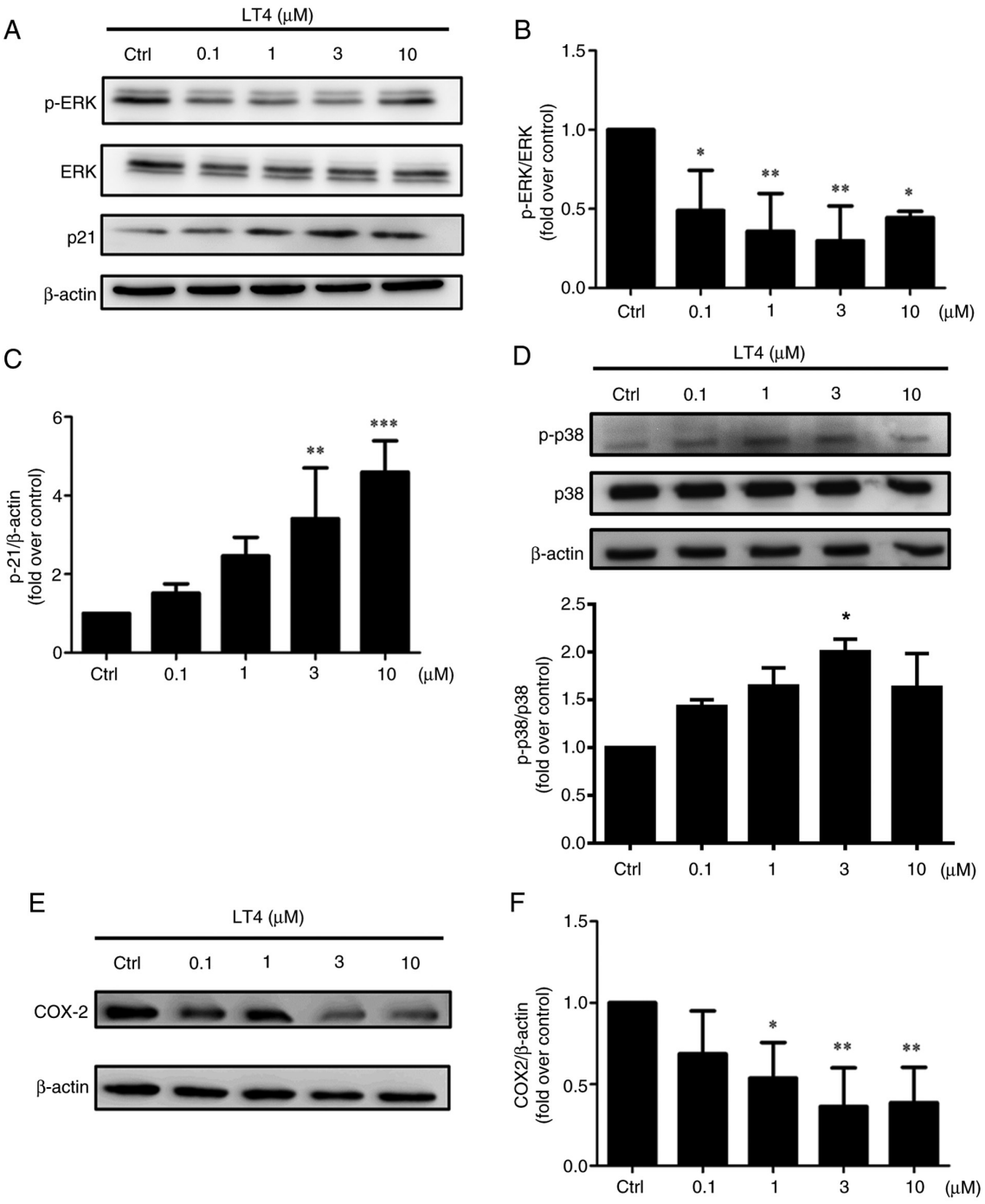

Figure 7. LT4 modulates the MAPK signaling pathway and suppresses COX-2 protein expression in HCT116 cells. HCT116 cells were treated with LT4 (0.1, 1, 3 and 10 μM) for 24 h. (A) Representative western blots of p-ERK1/2 (42/44 kDa), total ERK1/2 and p21 (21 kDa), with β-actin (45 kDa) as the loading control. (B) Densitometric quantification of p-ERK/ERK. (C) Densitometric quantification of p21/β-actin. (D) Representative western blots of p-p38 (43 kDa) and total p38 (40 kDa), with β-actin as the loading control, and corresponding densitometric quantification of p-p38/p38. (E) Representative western blot of COX-2 (74 kDa) with β-actin as the loading control. (F) Densitometric quantification of COX-2/β-actin. Data are presented as the mean ± SD from three independent experiments (n=3). Representative blots are shown; bar graphs represent densitometric quantification from three independent experiments (n=3), normalized to the indicated total protein or β-actin, and expressed as fold change relative to the vehicle-treated Ctrl. *P<0.05, **P<0.01, ***P<0.001 vs. vehicle-treated Ctrl. LT4, 4-acetylantrocamol LT3; p-, phosphorylated; Ctrl, control; COX-2, cyclooxygenase-2.

Lys-890 and positioning its long side chain within a hydrophobic pocket bordered by residues such as Ser806, Lys833, Ala885, Ile963 and Asp964 (Fig. 9C and D). LT4 adopted a binding position similar to antroquinonol, forming van der Waals contacts with Lys-833, a carbon-hydrogen bond with Val-882 and sharing interaction sites with residues Ile-963 and Asp-964 (Fig. 9E and F). These results suggested that LT4 may occupy the ATP pocket of PI3Kγ in a biologically relevant orientation.

Binding energy calculations showed that antroquinonol had the strongest predicted binding energy (-60.49±2.90 kcal/mol), significantly lower than that of LT4 (-44.50±4.01 kcal/mol; P=0.0047), whereas LT4 and KWT (-35.37±4.13 kcal/mol) were not significantly different (Fig. 9G). While LT4 did not

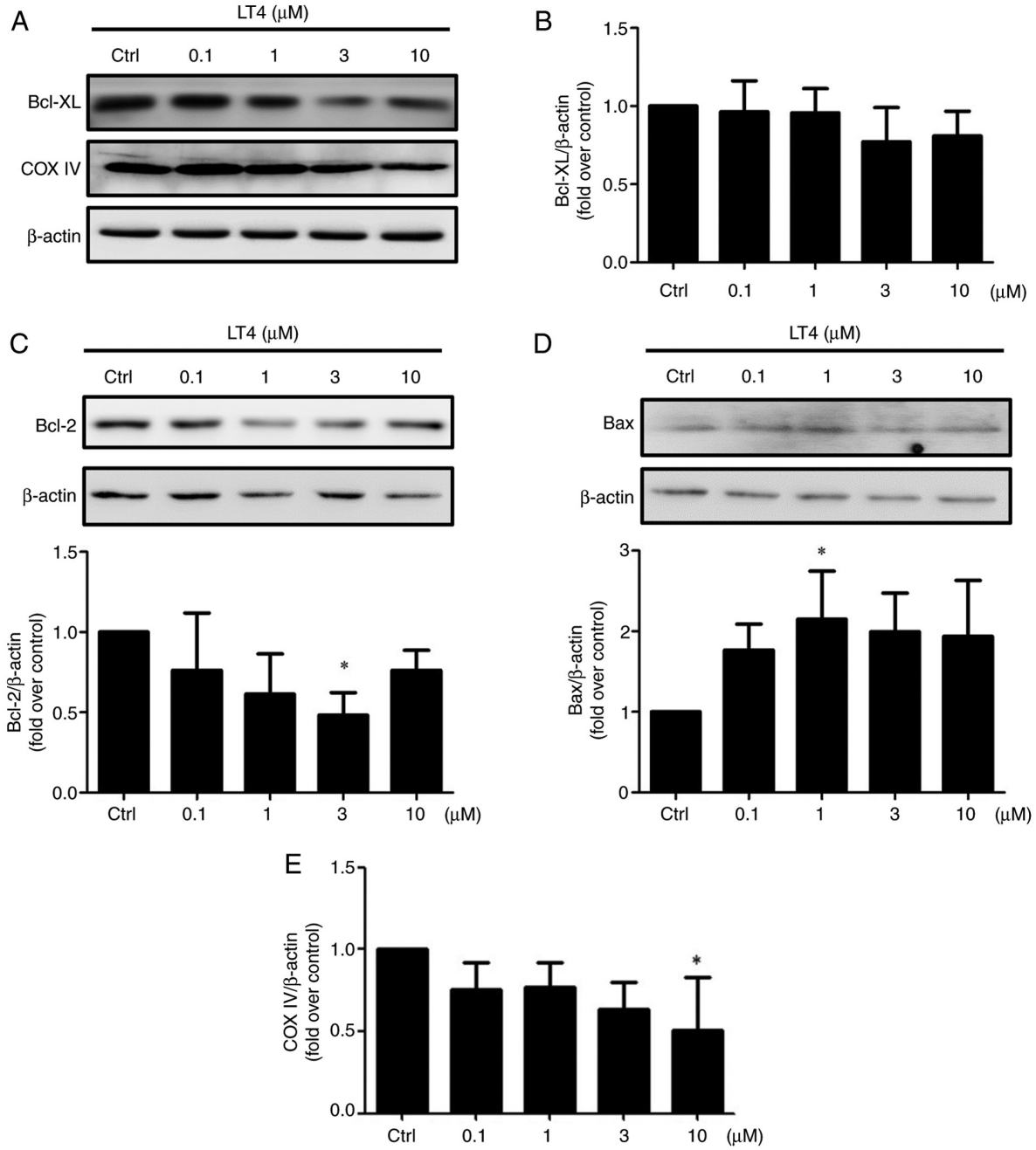

Figure 8. LT4 induces a pro-apoptotic shift in Bcl-2 family protein levels and reduces the levels of the mitochondrial marker, COX IV, in HCT116 cells. HCT116 cells were treated with LT4 (0.1, 1, 3 and 10 μM) for 24 h. (A) Representative immunoblots of Bcl-XL (30 kDa) and COX IV (17 kDa), with β-actin (45 kDa) serving as the loading control. (B) Densitometric quantification of Bcl-XL/β-actin. (C) Representative immunoblot and densitometric quantification of Bcl-2 (28 kDa)/β-actin. (D) Representative immunoblot and densitometric quantification of Bax (20 kDa)/β-actin. (E) Densitometric quantification of COX IV/β-actin. Data are presented as the mean ± SD from three independent experiments (n=3), normalized to β-actin and expressed as fold change relative to the vehicle-treated Ctrl. *P<0.05 vs. vehicle-treated Ctrl. LT4, 4-acetylantrocamol LT3; Ctrl, control; COX IV, cytochrome c oxidase subunit IV.

exhibit the most favorable predicted binding energy among the tested compounds, its consistent docking position and stable interaction profile within the PI3K active site support its potential to engage PI3K and contribute to downstream signaling inhibition, as observed in both transcriptomic and biochemical analyses.

Discussion

The present study comprehensively investigated the therapeutic potential and underlying mechanisms of LT4, a triterpenoid derivative from *A. cinnamomea* mycelium, in human CRC HCT116 cells. The data demonstrated that LT4 significantly suppressed cell viability, colony formation and cell migration, while inducing apoptosis-related signaling and decreasing the mitochondrial marker COX IV.

Studies have shown that *A. cinnamomea* extracts exert anti-CRC effects primarily through autophagy and apoptosis induction. For instance, a study demonstrated that *A. cinnamomea* activates the CHOP/TRB3/AKT/mTOR pathway to induce autophagic cell death in CRC cells (12), while another identified Antrodin C, a compound isolated from *A. cinnamomea*,

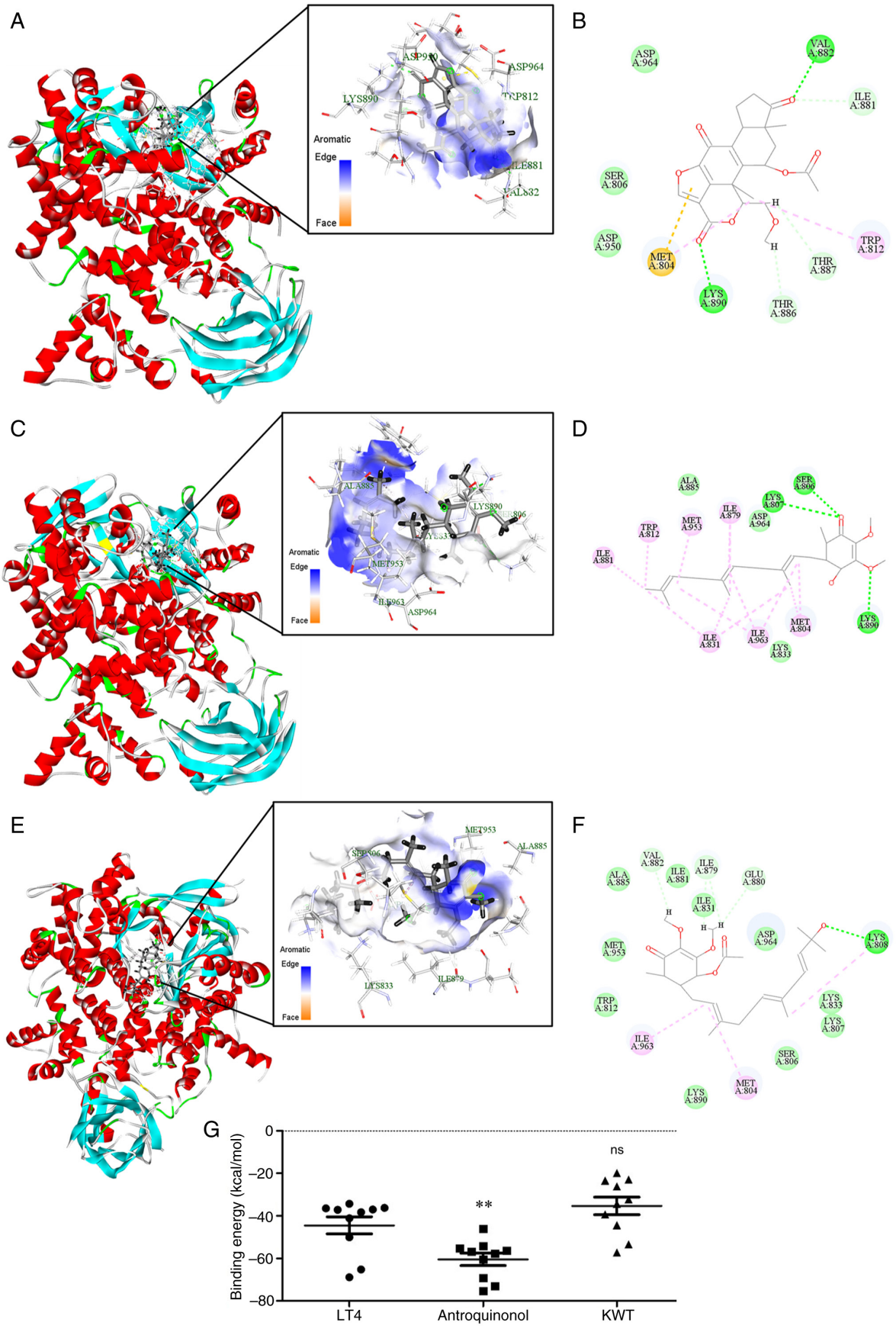

Figure 9. Molecular docking analysis of KWT, antroquinonol and LT4 with the ATP-binding site of PI3Kγ. (A) 3D docking position of KWT (wortmannin) in the PI3Kγ ATP-binding pocket (PDB: 1E7U); the inset shows a zoomed-in view of key binding residues. (B) 2D interaction map of KWT illustrating hydrogen bonds, van der Waals and hydrophobic interactions. (C) 3D docking position of antroquinonol with the corresponding (D) 2D interaction map. (E) 3D docking position of LT4 with the corresponding (F) 2D interaction map. (G) Scatter plots of the binding energies (kcal/mol) calculated for each compound (n=10 positions per ligand). Statistical comparisons were performed using an unpaired t-test: LT4 vs. antroquinonol, P=0.0047; LT4 vs. KWT, P=0.1301. **P<0.01. KWT, wortmannin; LT4, 4-acetylantrocamol LT3; ns, not significant.

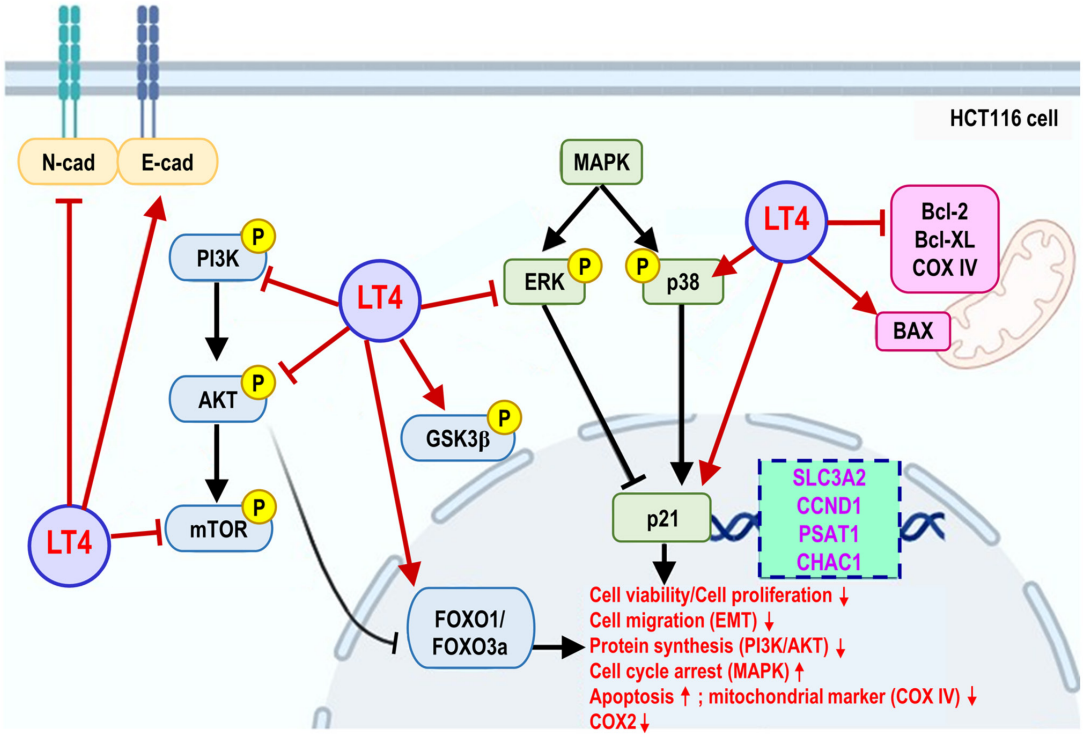

Figure 10. Proposed schematic model of LT4-mediated anticancer signaling regulation in HCT116 colorectal cancer cells. This schematic summarizes the proposed major pathways and regulatory nodes modulated by LT4, based on transcriptomic, western blotting and molecular docking analyses. LT4 inhibits the PI3K/AKT/mTOR signaling cascade, as reflected by reduced phosphorylation signaling and the annotated functional outcomes (cell viability/cell proliferation and protein synthesis). In addition, LT4 shifts EMT marker expression toward an epithelial phenotype (increased E-cadherin and decreased N-cadherin). In parallel, LT4 modulates the GSK3β-FOXO1/FOXO3a node and differentially regulates MAPK signaling by suppressing ERK phosphorylation while enhancing p38 activation, accompanied by p21 upregulation, consistent with cell-cycle arrest and stress-response phenotypes. LT4 also modulates apoptosis by decreasing the levels of anti-apoptotic proteins (Bcl-2 and Bcl-XL) and increasing Bax expression, alongside mitochondrial destabilization (COX IV) and COX-2 suppression. Key hub genes identified through protein-protein interaction network analysis, SLC3A2, CCND1, PSAT1 and CHAC1, are highlighted as potential mediators linking transcriptomic regulation to these functional outcomes. Black arrows indicate canonical interactions supported by previous studies; red arrows indicate regulatory effects supported by the experimental data in the present study; dashed lines indicate docking-predicted interactions. Arrows indicate activation, whereas blunt-ended lines indicate inhibition. LT4, 4-acetylantrocamol LT3; PI3K, phosphoinositide 3-kinase; AKT, protein kinase B; mTOR, mechanistic target of rapamycin; MAPK, mitogen-activated protein kinase; ERK, extracellular signal-regulated kinase; GSK3β, glycogen synthase kinase 3 β; FOXO, forkhead box O; BAX, COX IV, cytochrome c oxidase subunit IV; COX-2, cyclooxygenase-2; N-cad, N-cadherin; E-cad, E-cadherin; EMT, epithelial-mesenchymal transition; P, phosphorylation; SLC3A2, solute carrier family 3 member 2; CCND1, cyclin D1; PSAT1, phosphoserine aminotransferase 1; CHAC1, ChaC glutathione-specific γ-glutamylcyclotransferase 1.

as an apoptosis inducer via ROS/AKT/ERK/P38 signaling and histone acetylation of the TNFα promoter (19). However, mechanistic elucidation at the level of signaling network modulation and direct molecular targeting has been limited. Compared with prior findings, the present study is the first to integrate RNA-seq, KEGG/GO enrichment, PPI network mapping, western blot validation and molecular docking to elucidate the multi-target anti-CRC potential of LT4.

In the present study, transcriptomic profiling revealed enrichment of the PI3K/AKT signaling pathway, consistent with the western blot data, where LT4 significantly down-regulated p-PI3K, p-AKT and p-mTOR. These effects were accompanied by modulation of downstream effectors in the GSK3β-FOXO axis, including upregulation of tumor suppressors p21, FOXO3a and $p27^{kip1}$. In parallel, ERK suppression and p38/p21 upregulation within the MAPK cascade were identified, supporting a dual mechanism involving both proliferative inhibition and stress-induced cell cycle arrest. Notably, molecular docking validated PI3K as a potential direct target of LT4. LT4 occupied the same ATP-binding pocket as KWT, the classical PI3K inhibitor (PDB: 1E7U) (23), and demonstrated a stable binding profile similar to that of antroquinonol, another *A. cinnamomea*-derived compound. Although its binding energy was not as strong as antroquinonol, LT4 showed a more favorable docking energy than KWT, supporting its moderate but functionally relevant PI3K-targeting capacity.

In the present study, among the identified hub genes, SLC3A2 and CCND1 emerged as central nodes in the PPI network, both previously linked to CRC progression via nutrient signaling and cell cycle regulation (41,43). In line with this, LT4 was shown to inhibit EMT-associated markers, reversed cadherin switching and downregulate COX-2, an inflammatory effector downstream of PI3K and MAPK, reinforcing the pleiotropic nature of LT4-mediated inhibition.

Based on the full STRING-derived interaction network, combined with CytoHubba centrality scoring and MCODE clustering, PSAT1 and CHAC1 emerged as consistently high-ranking genes across multiple topological metrics in the present study, underscoring their potential functional importance in the LT4-regulated network. PSAT1 is a key enzyme in the serine biosynthesis pathway and its upregulation has been shown to promote CRC cell proliferation and metastasis through activation of the Hippo-YAP/TAZ-ID1 axis, independent of its metabolic activity (68). PSAT1 has also been implicated in chemoresistance

and is associated with poor prognosis in CRC (68-70). CHAC1 contributes to redox regulation by degrading glutathione and modulating oxidative stress. Elevated CHAC1 expression has been associated with ferroptosis induction and poor survival outcomes in several cancer types, including CRC (32,71).

The results of the present study also support the effect of LT4 on cell cycle regulation. Transcriptomic enrichment pointed to KEGG and GO terms related to cell cycle checkpoints and proliferation, while hub gene analysis identified CCND1 and PSAT1 as central regulators. These findings were functionally consistent with the observed induction of p21 and $p27^{kip1}$, both inhibitors of cyclin-dependent kinases, and suppression of CCND1 signaling. Taken together, these findings support a role for LT4 in cell-cycle regulatory perturbation, thereby restricting CRC cell proliferation in concert with the modulation of upstream PI3K/AKT and MAPK cascades, including the induction of FOXO3a and reduction of p-FOXO1 levels.

To further distill the mechanistic landscape of the effects of LT4, a summary schematic (Fig. 10) that integrates key signaling pathways and transcriptionally regulated nodes was constructed. This model highlights the ability of LT4 to interfere with PI3K/AKT/mTOR, GSK3β/FOXO, MAPK/p38 and apoptosis-related signaling cascades. The inclusion of PSAT1 and CHAC1 in this framework underscores their potential as novel downstream mediators of LT4's antitumor activity.

Limitations of the present study should be acknowledged. First, all functional assays were performed *in vitro*, and no *in vivo* xenograft models were included. Although the data consistently demonstrated that LT4 modulates PI3K/AKT/mTOR and MAPK signaling pathways in CRC cells, the lack of animal studies limits the extrapolation of these findings to complex tumor microenvironments. Future studies employing xenograft or patient-derived models will be required to validate the therapeutic relevance and pharmacokinetic properties of LT4 *in vivo*. Second, most mechanistic experiments were conducted in the HCT116 cell line, which harbors a KRAS mutation and served as a responsive model in the present study. While this approach provided consistent insights into the antitumor mechanisms of LT4, it did not capture the full spectrum of genetic heterogeneity in CRC. Validation in additional KRAS-mutant cell lines, or other genetically diverse CRC models, will be essential to strengthen the generalizability of these findings. Third, although network topology analysis consistently highlighted hub genes such as SLC3A2, PSAT1 and CHAC1, the present study did not include direct functional assays to establish their causal involvement in mediating the anticancer effects of LT4. These genes were identified bioinformatically as central regulators within the LT4-responsive network, but experimental knockdown or overexpression studies will be required to validate their mechanistic roles. Finally, although LT4 was shown to consistently suppress the phosphorylation of PI3K (p85 subunits) in HCT116 cells and molecular docking analysis supported PI3Kγ as a potential direct target of LT4, no functional confirmation was performed in the present study. Biochemical kinase and genetic approaches, such as PI3K overexpression or the expression of constitutively active mutants, would be required to verify direct PI3K engagement and to determine whether the inhibitory effects of LT4 are specifically mediated through PI3K.

In conclusion, to the best of our knowledge, the present study provides the first integrative evidence that LT4, a compound from *A. cinnamomea* mycelium, exerts anti-CRC activity by modulating multiple key signaling pathways, including PI3K/AKT/mTOR, GSK3β/FOXO, MAPK, apoptosis and COX-2. Through transcriptomic, biochemical and molecular docking validation, it was demonstrated that LT4 not only regulated signaling cascades at the transcriptional and protein levels but may also directly engage PI3K as a potential target. These findings establish LT4 as a promising candidate for further preclinical development in CRC therapy, particularly for tumors with KRAS mutations, where treatment options remain limited. Future studies are warranted to evaluate *in vivo* efficacy and to explore the combinatory potential of LT4 with conventional chemotherapies.

Acknowledgements

No applicable.

Funding

This work was supported by Grants from the Ministry of Science and Technology (grant no. MOST112-2320-B-016-005) and the Ministry of National Defense-Medical Affairs Bureau (grant nos. MND-MAB-109-051, MND-MAB-110-006, MND-MAB-D-112080, MND-MAB-D-113118 and MND-MAB-C01-114002).

Availability of data and materials

The RNA sequencing data generated in the present study may be found in the NCBI Gene Expression Omnibus database under the accession number GSE299648 or at the following URL: https://www.ncbi.nlm.nih.gov/geo/query/acc.cgi?acc=GSE299648. All other data generated in the present study may be requested from the corresponding author.

Authors' contributions

KTL conceived and designed the study, acquired the data, performed the analyses, interpreted the results, drafted the manuscript and approved the final version of the manuscript. YCH acquired the data, performed the analyses, interpreted the results and critically revised the manuscript. PKC and CWL acquired the data, performed the analyses and interpreted the results. SYL performed the analyses and interpreted the results. ICY interpreted the results, critically revised the manuscript and supervised the study. KTL and ICY confirm the authenticity of all the raw data. All authors read and approved the final version of the manuscript.

Ethics approval and consent to participate

Not applicable.

Patient consent for publication

Not applicable.

Competing interests

The authors declare that they have no competing interests.

References

1. Zhang T, Guo Y, Qiu B, Dai X, Wang Y and Cao X: Global, regional, and national trends in colorectal cancer burden from 1990 to 2021 and projections to 2040. Front Oncol 14: 1466159, 2025.
2. Teixeira N, Baião A, Dias S and Sarmento B: The progress and challenges in modeling colorectal cancer and the impact on novel drug discovery. Expert Opin Drug Discov 20: 565-574, 2025.
3. National Cancer Institute (NCI): Cancer stat facts: Colorectal cancer. In: Surveillance, Epidemiology, and End Results (SEER) Program. NCI, Bethesda, MD, 2025.
4. Leowattana W, Leowattana P and Leowattana T: Systemic treatment for metastatic colorectal cancer. World J Gastroenterol 29: 1569-1588, 2023.
5. Al Zein M, Boukhdoud M, Shammaa H, Mouslem H, El Ayoubi LM, Iratni R, Issa K, Khachab M, Assi HI, Sahebkar A and Eid AH: Immunotherapy and immunoevasion of colorectal cancer. Drug Discov Today 28: 103669, 2023.
6. Siena S, Sartore-Bianchi A, Di Nicolantonio F, Balfour J and Bardelli A: Biomarkers predicting clinical outcome of epidermal growth factor receptor-targeted therapy in metastatic colorectal cancer. J Natl Cancer Inst 101: 1308-1324, 2009.
7. Liebl MC and Hofmann TG: The role of p53 signaling in colorectal cancer. Cancers (Basel) 13: 2125, 2021.
8. Tang YL, Li DD, Duan JY, Sheng LM and Wang X: Resistance to targeted therapy in metastatic colorectal cancer: Current status and new developments. World J Gastroenterol 29: 926-948, 2023.
9. Wang CZ, Calway T and Yuan CS: Herbal medicines as adjuvants for cancer therapeutics. Am J Chin Med 40: 657-669, 2012.
10. Jenča A, Mills DK, Ghasemi H, Saberian E, Jenča A, Karimi Forood AM, Petrášová A, Jenčová J, Jabbari Velisdeh Z, Zare-Zardini H and Ebrahimifar M: Herbal therapies for cancer treatment: A review of phytotherapeutic efficacy. Biologics 18: 229-255, 2024.
11. Lu MC, El-Shazly M, Wu TY, Du YC, Chang TT, Chen CF, Hsu YM, Lai KH, Chiu CP, Chang FR and Wu YC: Recent research and development of *Antrodia cinnamomea*. Pharmacol Ther 139: 124-156, 2013.
12. Tsai DH, Chung CH and Lee KT: *Antrodia cinnamomea* induces autophagic cell death via the CHOP/TRB3/Akt/mTOR pathway in colorectal cancer cells. Sci Rep 8: 17424, 2018.
13. Huang YJ, Yadav VK, Srivastava P, Wu AT, Huynh TT, Wei PL, Huang CF and Huang TH: *Antrodia cinnamomea* Enhances chemo-sensitivity of 5-FU and suppresses colon tumorigenesis and cancer stemness via up-regulation of tumor suppressor miR-142-3p. Biomolecules 9: 306, 2019.
14. Lin IY, Pan MH, Lai CS, Lin TT, Chen CT, Chung TS, Chen CL, Lin CH, Chuang WC, Lee MC, *et al*: CCM111, the water extract of *Antrodia cinnamomea*, regulates immune-related activity through STAT3 and NF-κB pathways. Sci Rep 7: 4862, 2017.
15. Liu YM, Liu YK, Huang PI, Tsai TH and Chen YJ: *Antrodia cinnamomea* mycelial fermentation broth inhibits the epithelial-mesenchymal transition of human esophageal adenocarcinoma cancer cells. Food Chem Toxicol 119: 380-386, 2018.
16. Li HX, Wang JJ, Lu CL, Gao YJ, Gao L and Yang ZQ: Review of bioactivity, isolation, and identification of active compounds from *Antrodia cinnamomea*. Bioengineering (Basel) 9: 494, 2022.
17. Senthil Kumar KJ, Gokila Vani M, Chen CY, Hsiao WW, Li J, Lin ZX, Chu FH, Yen GC and Wang SY: A mechanistic and empirical review of antcins, a new class of phytosterols of formosan fungi origin. J Food Drug Anal 28: 38-59, 2020.
18. Lee YP, Tsai WC, Ko CJ, Rao YK, Yang CR, Chen DR, Yang MH, Yang CC and Tzeng YM: Anticancer effects of eleven triterpenoids derived from Antrodia camphorata. Anticancer Res 32: 2727-2734, 2012.
19. Hsieh YY, Lee KC, Cheng KC, Lee KF, Yang YL, Chu HT, Lin TW, Chen CC, Hsieh MC, Huang CY, *et al*: Antrodin C isolated from *Antrodia cinnamomea* induced apoptosis through ROS/AKT/ERK/P38 signaling pathway and epigenetic histone acetylation of TNFα in colorectal cancer cells. Antioxidants (Basel) 12: 764, 2023.
20. Chen S, Zhou Y, Chen Y and Gu J: fastp: An ultra-fast all-in-one FASTQ preprocessor. Bioinformatics 34: i884-i890, 2018.
21. Love MI, Huber W and Anders S: Moderated estimation of fold change and dispersion for RNA-seq data with DESeq2. Genome Biol 15: 550, 2014.
22. Yu G, Wang LG, Han Y and He QY: clusterProfiler: An R package for comparing biological themes among gene clusters. OMICS 16: 284-287, 2012.
23. Walker EH, Pacold ME, Perisic O, Stephens L, Hawkins PT, Wymann MP and Williams RL: Structural determinants of phosphoinositide 3-kinase inhibition by wortmannin, LY294002, quercetin, myricetin, and staurosporine. Mol Cell 6: 909-919, 2000.
24. Loh CY, Chai JY, Tang TF, Wong WF, Sethi G, Shanmugam MK, Chong PP and Looi CY: The E-cadherin and N-cadherin switch in epithelial-to-mesenchymal transition: Signaling, therapeutic implications, and challenges. Cells 8: 1118, 2019.
25. Du L, Li J, Lei L, He H, Chen E, Dong J and Yang J: High vimentin expression predicts a poor prognosis and progression in colorectal cancer: A study with meta-analysis and TCGA database. Biomed Res Int 2018: 6387810, 2018.
26. Kim TW, Lee YS, Yun NH, Shin CH, Hong HK, Kim HH and Cho YB: MicroRNA-17-5p regulates EMT by targeting vimentin in colorectal cancer. Br J Cancer 123: 1123-1130, 2020.
27. Niknami Z, Muhammadnejad A, Ebrahimi A, Harsani Z and Shirkoohi R: Significance of E-cadherin and vimentin as epithelial-mesenchymal transition markers in colorectal carcinoma prognosis. EXCLI J 19: 917-926, 2020.
28. Emile MH, Emile SH, El-Karef AA, Ebrahim MA, Mohammed IE and Ibrahim DA: Association between the expression of epithelial-mesenchymal transition (EMT)-related markers and oncologic outcomes of colorectal cancer. Updates Surg 76: 2181-2191, 2024.
29. Kahya U, Köseer AS and Dubrovska A: Amino acid transporters on the guard of cell genome and epigenome. Cancers (Basel) 13: 125, 2021.
30. Bröer A, Rahimi F and Bröer S: Deletion of amino acid transporter ASCT2 (SLC1A5) reveals an essential role for transporters SNAT1 (SLC38A1) and SNAT2 (SLC38A2) to sustain glutaminolysis in cancer cells. J Biol Chem 291: 13194-13205, 2016.
31. Wu D and Liang J: Activating transcription factor 4: A regulator of stress response in human cancers. Front Cell Dev Biol 12: 1370012, 2024.
32. Sun J, Ren H, Wang J, Xiao X, Zhu L, Wang Y and Yang L: CHAC1: A master regulator of oxidative stress and ferroptosis in human diseases and cancers. Front Cell Dev Biol 12: 1458716, 2024.
33. Gao S, Ge A, Xu S, You Z, Ning S, Zhao Y and Pang D: PSAT1 is regulated by ATF4 and enhances cell proliferation via the GSK3β/β-catenin/cyclin D1 signaling pathway in ER-negative breast cancer. J Exp Clin Cancer Res 36: 179, 2017.
34. Martens-de Kemp SR, Brink A, Stigter-van Walsum M, Damen JM, Rustenburg F, Wu T, van Wieringen WN, Schuurhuis GJ, Braakhuis BJ, Slijper M and Brakenhoff RH: CD98 marks a subpopulation of head and neck squamous cell carcinoma cells with stem cell properties. Stem Cell Res 10: 477-488, 2013.
35. Fei F, Li X, Xu L, Li D, Zhang Z, Guo X, Yang H, Chen Z and Xing J: CD147-CD98hc complex contributes to poor prognosis of non-small cell lung cancer patients through promoting cell proliferation via the PI3K/Akt signaling pathway. Ann Surg Oncol 21: 4359-4368, 2014.
36. Kaira K, Sunose Y, Oriuchi N, Kanai Y and Takeyoshi I: CD98 is a promising prognostic biomarker in biliary tract cancer. Hepatobiliary Pancreat Dis Int 13: 654-657, 2014.
37. Furuya M, Horiguchi J, Nakajima H, Kanai Y and Oyama T: Correlation of L-type amino acid transporter 1 and CD98 expression with triple negative breast cancer prognosis. Cancer Sci 103: 382-389, 2012.
38. Zhu B, Cheng D, Hou L, Zhou S, Ying T and Yang Q: SLC3A2 is upregulated in human osteosarcoma and promotes tumor growth through the PI3K/Akt signaling pathway. Oncol Rep 37: 2575-2582, 2017.
39. Xia P and Dubrovska A: CD98 heavy chain as a prognostic biomarker and target for cancer treatment. Front Oncol 13: 1251100, 2023.
40. Shin DH, Jo JY and Han JY: Dual targeting of ERBB2/ERBB3 for the treatment of SLC3A2-NRG1-mediated lung cancer. Mol Cancer Ther 17: 2024-2033, 2018.
41. Huang G, Ma L, Shen L, Lei Y, Guo L, Deng Y and Ding Y: MIF/SCL3A2 depletion inhibits the proliferation and metastasis of colorectal cancer cells via the AKT/GSK-3β pathway and cell iron death. J Cell Mol Med 26: 3410-3422, 2022.

42. Ortiz AB, Garcia D, Vicente Y, Palka M, Bellas C and Martin P: Prognostic significance of cyclin D1 protein expression and gene amplification in invasive breast carcinoma. PLoS One 12: e0188068, 2017.
43. Jun SY, Kim J, Yoon N, Maeng LS and Byun JH: Prognostic potential of cyclin D1 expression in colorectal cancer. J Clin Med 12: 572, 2023.
44. Shan YS, Hsu HP, Lai MD, Hung YH, Wang CY, Yen MC and Chen YL: Cyclin D1 overexpression correlates with poor tumor differentiation and prognosis in gastric cancer. Oncol Lett 14: 4517-4526, 2017.
45. Guo Z, Liang E, Li W, Jiang L and Zhi F: Essential meiotic structure-specific endonuclease1 (EME1) promotes malignant features in gastric cancer cells via the Akt/GSK3B/CCND1 pathway. Bioengineered 12: 9869-9884, 2021.
46. Maharati A and Moghbeli M: PI3K/AKT signaling pathway as a critical regulator of epithelial-mesenchymal transition in colorectal tumor cells. Cell Commun Signal 21: 201, 2023.
47. Almaimani RA, Aslam A, Ahmad J, El-Readi MZ, El-Boshy ME, Abdelghany AH, Idris S, Alhadrami M, Althubiti M, Almasmoum HA, *et al*: In vivo and in vitro enhanced tumoricidal effects of metformin, active vitamin D_3, and 5-fluorouracil triple therapy against colon cancer by modulating the PI3K/Akt/PTEN/mTOR network. Cancers (Basel) 14: 1538, 2022.
48. Currier AW, Kolb EA, Gorlick RG, Roth ME, Gopalakrishnan V and Sampson VB: p27/Kip1 functions as a tumor suppressor and oncoprotein in osteosarcoma. Sci Rep 9: 6161, 2019.
49. Liu Y, Ao X, Ding W, Ponnusamy M, Wu W, Hao X, Yu W, Wang Y, Li P and Wang J: Critical role of FOXO3a in carcinogenesis. Mol Cancer 17: 104, 2018.
50. Kim GY, Mercer SE, Ewton DZ, Yan Z, Jin K and Friedman E: The stress-activated protein kinases p38 alpha and JNK1 stabilize p21(Cip1) by phosphorylation. J Biol Chem 277: 29792-29802, 2002.
51. Lafarga V, Cuadrado A, Lopez de Silanes I, Bengoechea R, Fernandez-Capetillo O and Nebreda AR: p38 Mitogen-activated protein kinase- and HuR-dependent stabilization of p21(Cip1) mRNA mediates the G(1)/S checkpoint. Mol Cell Biol 29: 4341-4351, 2009.
52. Hwang CY, Lee C and Kwon KS: Extracellular signal-regulated kinase 2-dependent phosphorylation induces cytoplasmic localization and degradation of p21Cip1. Mol Cell Biol 29: 3379-3389, 2009.
53. Kumari G, Ulrich T and Gaubatz S: A role for p38 in transcriptional elongation of p21 (CIP1) in response to Aurora B inhibition. Cell Cycle 12: 2051-2060, 2013.
54. Chang J, Tang N, Fang Q, Zhu K, Liu L, Xiong X, Zhu Z, Zhang B, Zhang M and Tao J: Inhibition of COX-2 and 5-LOX regulates the progression of colorectal cancer by promoting PTEN and suppressing PI3K/AKT pathway. Biochem Biophys Res Commun 517: 1-7, 2019.
55. Yoshitake R, Saeki K, Eto S, Shinada M, Nakano R, Sugiya H, Endo Y, Fujita N, Nishimura R and Nakagawa T: Aberrant expression of the COX2/PGE2 axis is induced by activation of the RAF/MEK/ERK pathway in $BRAF^{V595E}$ canine urothelial carcinoma. Sci Rep 10: 7826, 2020.
56. Sheng J, Sun H, Yu FB, Li B, Zhang Y and Zhu YT: The role of cyclooxygenase-2 in colorectal cancer. Int J Med Sci 17: 1095-1101, 2020.
57. Cai B, Chang SH, Becker EB, Bonni A and Xia Z: p38 MAP kinase mediates apoptosis through phosphorylation of BimEL at Ser-65. J Biol Chem 281: 25215-25222, 2006.
58. Wakeman D, Guo J, Santos JA, Wandu WS, Schneider JE, McMellen ME, Leinicke JA, Erwin CR and Warner BW: p38 MAPK regulates Bax activity and apoptosis in enterocytes at baseline and after intestinal resection. Am J Physiol Gastrointest Liver Physiol 302: G997-G1005, 2012.
59. Bodur C, Kutuk O, Karsli-Uzunbas G, Isimjan TT, Harrison P and Basaga H: Pramanicin analog induces apoptosis in human colon cancer cells: Critical roles for Bcl-2, Bim, and p38 MAPK signaling. PLoS One 8: e56369, 2013.
60. Zhang X, Tang N, Hadden TJ and Rishi AK: Akt, FoxO and regulation of apoptosis. Biochim Biophys Acta 1813: 1978-1986, 2011.
61. Das TP, Suman S, Alatassi H, Ankem MK and Damodaran C: Inhibition of AKT promotes FOXO3a-dependent apoptosis in prostate cancer. Cell Death Dis 7: e2111, 2016.
62. Yun SI, Yoon HY and Chung YS: Glycogen synthase kinase-3beta regulates etoposide-induced apoptosis via Bcl-2 mediated caspase-3 activation in C3H10T1/2 cells. Apoptosis 14: 771-777, 2009.
63. Lin J, Song T, Li C and Mao W: GSK-3β in DNA repair, apoptosis, and resistance of chemotherapy, radiotherapy of cancer. Biochim Biophys Acta Mol Cell Res 1867: 118659, 2020.
64. Yang K, Chen Z, Gao J, Shi W, Li L, Jiang S, Hu H, Liu Z, Xu D and Wu L: The key roles of GSK-3β in regulating mitochondrial activity. Cell Physiol Biochem 44: 1445-1459, 2017.
65. Li Y, Park JS, Deng JH and Bai Y: Cytochrome c oxidase subunit IV is essential for assembly and respiratory function of the enzyme complex. J Bioenerg Biomembr 38: 283-291, 2006.
66. Lin HC, Lin MH, Liao JH, Wu TH, Lee TH, Mi FL, Wu CH, Chen KC, Cheng CH and Lin CW: Antroquinonol, a ubiquinone derivative from the mushroom antrodia camphorata, inhibits colon cancer stem cell-like properties: Insights into the molecular mechanism and inhibitory targets. J Agric Food Chem 65: 51-59, 2017.
67. Angamuthu V, Shanmugavadivu M, Nagarajan G and Velmurugan BK: Pharmacological activities of antroquinonol-mini review. Chem Biol Interact 297: 8-15, 2019.
68. Tang M, Song K, Xie D, Yuan X, Wang Y, Li Z, Lu X, Guo L, Zhu X, Xiong L, *et al*: PSAT1 promotes the progression of colorectal cancer by regulating Hippo-YAP/TAZ-ID1 axis via AMOT. Mol Cell Biochem 480: 3647-3668, 2025.
69. Vié N, Copois V, Bascoul-Mollevi C, Denis V, Bec N, Robert B, Fraslon C, Conseiller E, Molina F, Larroque C, *et al*: Overexpression of phosphoserine aminotransferase PSAT1 stimulates cell growth and increases chemoresistance of colon cancer cells. Mol Cancer 7: 14, 2008.
70. Wang M, Zhang H, Lu Z, Su W, Tan Y, Wang J and Jia X: PSAT1 mediated EMT of colorectal cancer cells by regulating Pl3K/AKT signaling pathway. J Cancer 15: 3183-3198, 2024.
71. Zhao X and Chen F: Propofol induces the ferroptosis of colorectal cancer cells by downregulating STAT3 expression. Oncol Lett 22: 767, 2021.